Dal Bello, R.; Martins, PM.; Brons, S.; Hermann, G.; Kihm, T.; Seimetz, M.; Seco, J. (2020). Prompt gamma spectroscopy for absolute range verification of 12C ions at synchroton-based facilities. Physics in Medicine and Biology. 65(9):1-23. https://doi.org/10.1088/1361-6560/ab7973

Prompt Gamma Spectroscopy for absolute range verification of ^{12}C ions at synchrotron based facilities

Riccardo Dal Bello

Division of Biomedical Physics in Radiation Oncology, German Cancer Research Center (DKFZ), Heidelberg, Germany
Department of Physics and Astronomy, Heidelberg University, Heidelberg, Germany

Paulo Magalhaes Martins

Division of Biomedical Physics in Radiation Oncology, German Cancer Research Center (DKFZ), Heidelberg, Germany
Instituto de Biofísica e Engenharia Biomédica, Faculdade de Cîencias, Universidade de Lisboa, Lisboa, Portugal

Stephan Brons

Heidelberg Ion-Beam Therapy Center (HIT), Heidelberg, Germany

German Hermann

Max-Planck-Institute for Nuclear Physics, Heidelberg, Germany

Thomas Kihm

Max-Planck-Institute for Nuclear Physics, Heidelberg, Germany

Michael Seimetz

Instituto de Instrumentación para Imagen Molecular (I3M), CSIC-Universitat Politècnica de València, Valencia, Spain

Joao Seco

Division of Biomedical Physics in Radiation Oncology, German Cancer Research Center (DKFZ), Heidelberg, Germany
Department of Physics and Astronomy, Heidelberg University, Heidelberg, Germany

E-mail: r.dalbello@dkfz.de

July 2019

Abstract.

The physical range uncertainty limits the exploitation of the full potential of charged particle therapy. In this work we face this issue aiming to measure the absolute Bragg peak position in the target. We investigate p, ^{4}He, ^{12}C and ^{16}O beams accelerated at the Heidelberg Ion-Beam Therapy Center. The residual range of the primary ^{12}C ions is correlated to the energy spectrum of the prompt gamma radiation. The prompt gamma spectroscopy method was demonstrated for proton beams accelerated by cyclotrons and is developed here for the first time for heavier ions accelerated by a synchrotron. We develop a detector system that includes (i) a spectroscopic unit based on cerium(III) bromide and bismuth germanium oxide scintillating crystals, (ii) a beam trigger based on an array of scintillating fibers and (iii) a data acquisition system based on a FlashADC. We test the system in two different scenarios. In the first series of experiments we detect and identify 19 independent spectral lines over a wide gamma energy spectrum in presence of the four ion species for different targets, including also a water target with a titanium insert. In the second series of experiments we introduce a collimator aiming to relate the spectral information to the range of the primary particles. We perform extensive measurements for a ^{12}C beam and demonstrate submillimetric precision for the measurement of its Bragg peak position in the experimental setup. The features of the energy and time spectra for gamma radiation induced by p, ^{4}He and ^{16}O are investigated upstream and downstream the Bragg peak position. We conclude the analysis extrapolating the required future developments, which would be needed to achieve range verification with a 2 mm accuracy during a single fraction delivery of $D = 2$ Gy physical dose.

Keywords: prompt gamma, range verification, proton therapy, ion beam therapy, charged particle therapy, radiotherapy, Heidelberg Ion-Beam Therapy Center

Submitted to: *Phys. Med. Biol.*

1. Introduction

The growing interest for charged particle therapy (CPT) is driven by the favorable depth-dose distribution of relativistic light ions in matter. Their energy deposition profile is referred to as Bragg peak and presents its maximum at the end of the range of the primary particles (Bragg et al., 1905). Such characteristic potentially allows the delivery of highly conformal radiation to the tumor while reducing the dose in the surrounding tissue (Amaldi et al., 2005). The number of patients receiving CPT is rapidly growing and it overcame the 200'000 treatments at the end of 2018 (PTCOG, 2018). This includes the clinical practice with p and ^{12}C beams and a pilot project that until 1992 treated over 2'000 patients with ^{4}He beams at Berkeley. The latter has recently gained new interest and the introduction of therapeutic ^{4}He beams has been planned at the Heidelberg Ion-Beam Therapy Center (HIT) for the next year (Mein et al., 2019). Moreover, additionally to the previously mentioned ion species, beams of ^{16}O ions are available for experimentation at HIT since they are considered attractive for the treatment of hypoxic tumors (Tommasino et al., 2015). The multiple ion species have separate rationales for their use, different biological properties, specific nuclear fragmentation processes and unique mixed fields. While proton beams can be accelerated also by cyclotron facilities, the availability of slightly relativistic ^{4}He, ^{12}C and ^{16}O beams is limited to synchrotrons. This property calls for the need of developing a device employable at synchrotron based facilities. Several new challenges are encountered in such case. First, synchrotrons are known to have lower beam intensities compared to cyclotrons (Krimmer et al., 2018). This could facilitate the prompt gamma detection and soften the throughput requirements of the photon detector. On the other hand, the time micro-structure of the synchrotron beam is less regular and the wide time extension of the bunches does not allow to perform an efficient rejection of the neutron-induced background using only the techniques proposed by Verburg et al., 2013; as also discussed by Krimmer et al., 2018.

Numerous solutions have been proposed to measure the range of the primary ions in vivo. Knopf et al., 2013 provide an overview on how particle treatments would benefit from an in vivo range verification system. They also analyze all the proposed techniques and show that exclusively one of these provides for all the body sites simultaneously a direct signal during CPT combined with an expected millimetric accuracy: prompt gamma imaging (PGI). This technique is based on the production of excited nuclear states through inelastic collisions of the projectiles with the target nuclei. Such states have typical mean life shorter than $\tau < 10^{-11}$ s and can de-excite with isomeric transitions emitting discrete gamma quanta with energy equal to the difference of the nuclear levels (Kozlovsky et al., 2002). The detection of this secondary radiation provides a non-invasive solution to measure the Bragg peak position without extra dose to the patient and without extending the treatment time. Therefore, several efforts have been undertaken to investigate PGI and multiple detection techniques are currently under development (Krimmer et al., 2018). Richter et al., 2016 acquired the first prompt

gamma data during proton treatments with passively scattered beams and Xie et al., 2017 investigated it during patient treatments with proton pencil beam scanning. In both cases, the detection aimed at retrieving relative shifts. The recovery of the absolute Bragg peak position for proton beams accelerated by cyclotrons was demonstrated by Verburg et al., 2014. This required the employment of large crystals with spectroscopy capability to measure multiple prompt gamma lines associated with independent de-excitation channels. This technique is referred to as prompt gamma spectroscopy (PGS). Hueso-González et al., 2018 recently presented a full scale prototype dedicated to PGS for proton beams accelerated by cyclotrons. They demonstrated the measurement of absolute millimetric deviations under clinically realistic conditions. Kelleter et al., 2017 investigated in thin-target experiments the prompt gamma spectrum emitted by protons accelerated at a synchrotron facility. In the current work we aim to develop PGS to heavier ions, with a special focus on ^{12}C beams, accelerated by synchrotrons.

The core of PGS is the capability to detect discrete spectral lines. Therefore, in a previous work a spectroscopic unit based on a cerium(III) bromide ($CeBr_3$) scintillating crystal was optimized (Dal Bello et al., 2018) . The choice of this scintillator was driven by the absence of intrinsic activity and its excellent time and energy resolution (Quarati et al., 2013). The possibility to detect the prompt gamma over its full energy spectrum down to $E_\gamma = 511$ keV is beneficial to include a multitude of independent reactions in the analysis and it was demonstrated during p experiments (Magalhaes Martins et al., 2017) and ^{4}He irradiation (Dal Bello et al., 2019). However, new challenges are encountered moving to heavier ions (Pinto et al., 2015). Testa et al., 2010 investigated the time structure of the secondary radiation generated by ^{12}C beams. For low energy pulsed beams there is a strong correlation with the accelerator high-frequency (HF) and the background rejection techniques adopted with p beams can be applied (Verburg et al., 2013). The correlation with the HF is lost for continuous beams at the high energies required for treatments. In this case the direct detection of the arrival time of the primary ions is necessary. Therefore, we developed a beam trigger based on scintillating fibers that provides minimal interaction with the beam, single particle measurement at high intensities and which is scalable to the maximum intensities used during treatments (Magalhaes Martins et al., 2019). Finally, the use of heavier ions is also associated with the production of nuclear fragments and higher neutron yield (Aricò et al., 2019). Such processes increase the noise in the detectors used for PGI and require the development of dedicated background rejection techniques. We take into account all the previous phenomena and aim to demonstrate that an absolute range verification with a precision of 2 mm is theoretically feasible. Such value is chosen to be smaller than the current physical range uncertainties, which can reach and exceed the 10 mm (Paganetti, 2012).

In this work, we investigate for the first time at a synchrotron based facility PGS for absolute range verification for ^{12}C beams. The features of prompt gamma energy and time spectra induced by the other beam species are also presented. The manuscript is divided in multiple sections with different focuses:

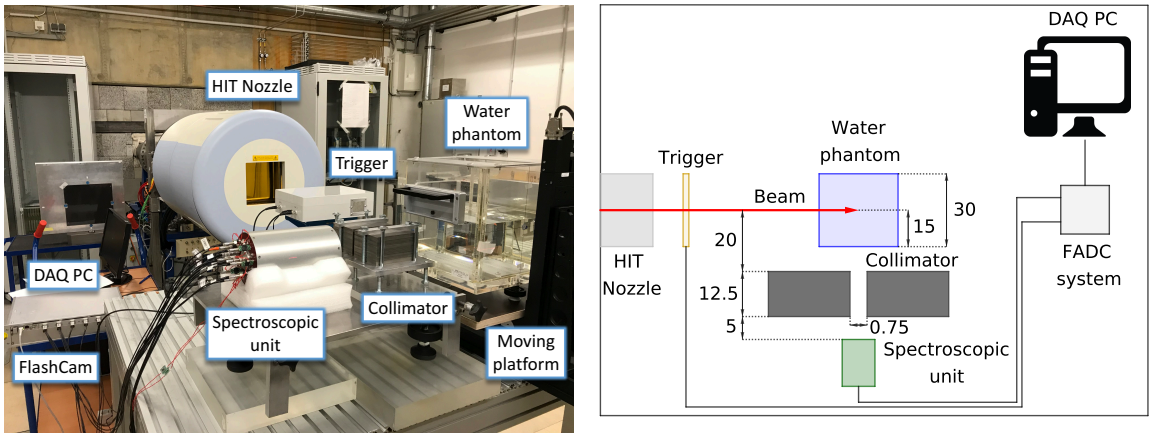

Figure 1. Left: Experimental setup in the cave at HIT. Right: Its schematic not to scale representation with labels indicating the distances between the components in centimeters.

- Section 2 presents the detectors and the data acquisition system adopted. The core of the system is the spectroscopic unit, which is used along with two beam triggers. The data acquisition is performed with a multichannel waveform digitizer.
- Section 3 explains the details of the data analysis. This includes the Monte Carlo characterization of the spectroscopic unit, the background suppression with secondary detectors and with a time-of-flight model.
- Section 4 describes the experimental campaigns. Two sets of experiments were performed. The uncollimated ones aimed to define the reaction channels measurable with the system. Then, in the second campaign, a collimator was introduced to correlate the prompt gamma spectral features to the Bragg peak position.

Finally, the remaining sections present the results and the discussion of this work.

2. Detectors and data acquisition system

The applicability of PGS for ion beam therapy in a synchrotron based facility was experimentally investigated. The current section presents the details of the experimental components.

2.1. Spectroscopic unit

The core of the experimental setup was the spectroscopic unit. The primary detector was a cerium bromide ($CeBr_3$) crystal with a cylindrical shape (diameter $d = 3.81$ cm and length $l = 7.62$ cm) coupled to a R9420-100 PMT (Hamamatsu). It was surrounded by a secondary bismuth germanium oxide (BGO) crystal with a cylindrical shape and a cavity to host the $CeBr_3$ (thickness $t = 3$ cm, length $l = 11$ cm and inner diameter $d_{\text{in}} = 4.6$ cm). The BGO was sectioned in eight azimuthally-symmetric and optically-separated segments. Each section was coupled to an independent

R1924 PMT (Hamamatsu). This crystal was used as Anti-Coincidence (AC) shield. The experimental performances of the spectroscopic unit in presence of ^{4}He beams accelerated at a clinical facility have been investigated in a previous dedicated study by Dal Bello et al., 2019. Figure 1 (left) shows the experimental setup with the spectroscopic unit at the center, behind the collimator.

2.2. Beam trigger

Two separate detectors have been used to measure the arrival time of primary particles in the experimental campaigns: the first was based on a plastic scintillator tile and the second on an array of scintillating fibers.

The plastic scintillator was 0.1 cm thick and covered a 8×8 cm^2 area. The tile was a EJ-200 plastic scintillator. It was connected on one side to a R13089 PMT (Hamamatsu) with a silicone coupling component. The tile was sealed with an aluminum foil to enhance the internal reflection and black tape to make it light tight. The same detector has been adopted also in a previous study (Dal Bello et al., 2019). This is further referred to as the *EJ-200 detector*. The total thickness of this detector was above the millimeter, which makes it suitable for experimental setups but inappropriate for clinical scenarios. Therefore, a further detector was developed and presented in the following paragraph.

The second beam trigger was based on a set of scintillating fibers with a square cross section of side length 500 μm. We designed dedicated supports to obtain a single layer of scintillating fibers (BCF-12, Saint Gobain Crystals). The total active area was 3×3 cm^2. The fibers were connected on one side to two independent R647 PMT with E849-35 socket assembly (Hamamatsu) in an alternating fashion. The detector included a housing for light shielding equipped with an entrance and exit window for the beam. Additionally to the 500 μm thickness of the scintillating material, the windows made of double aluminized mylar had a thickness of < 10 μm, leading to a total thickness of the detector in beam direction of < 510 μm. This detector was designed to be operated at higher intensities compared to the EJ-200 and its experimental performances in presence of clinical ion beams have been investigated in a previous dedicated study by Magalhaes Martins et al., 2019. This is further referred to as the *SciFi detector*. Figure 1 (left) shows the SciFi detector at the front of the experimental setup, between the nozzle and the water phantom.

The main purpose of the beam triggers was to provide the time information to derive the ToF model. When comparing the detectors, the signal decay times of the scintillators EJ-200 and BCF-12, respectively $\tau_{\text{EJ-200}} = 2.1$ ns and $\tau_{\text{BCF-12}} = 3.2$ ns, are approximately one order of magnitude faster than the one of the $CeBr_3$ ($\tau_{CeBr_3} = 20$ ns). Therefore, the latter dominates the time resolution of the system. Magalhaes Martins et al., 2019 demonstrated a subnanosecond (FWHM = 0.8 ns) time resolution in the coincidence signal detection, which makes this system suitable for the development of a ToF model based on sampling intervals of few nanoseconds. Finally, the time resolution

of the BGO does not have a direct influence on the ToF model. Its signal decay time ($\tau_{\mathrm{BGO}} = 300$ ns) allows data acquisition with pile-up smaller than 1.5% at the maximum count rates observed in this study. Dal Bello et al., 2019 presented a resolution in the coincidence signal detection between the $CeBr_3$ and the BGO of FWHM = 3.58 ns.

2.3. Electronics

A transient recorder was used for the digitalization of the detector signals (Werner et al., 2017). Such system was originally developed for the Cerenkov Telescope Array and is highly flexible and promptly adaptable to PGS experiments. Three fundamental properties made the FlashCam modules especially suitable for the current work: the Ethernet-based interface (1 Gbit) with high data-rate capability for continuous data streaming, multi-channel acquisition mode and the continuous high-speed digitization (12-bit, 250 MS/s FADC system) with on-board FPGA-based digital signal processing and triggering. Figure 1 (left) shows the FlashCam module at the side of the experimental setup.

The data acquisition system (DAQ) was operated with up to $N_{\mathrm{ch}} = 17$ independent channels for which the signal was continuously digitized and processed by an on-board FPGA to derive a trigger signal when energy depositions in the $CeBr_3$ of $E \geq 500$ keV happened. Every channel acquired event-by-event single traces $\Delta t = 240$ ns long. The sampling intervals were chosen depending on the detector properties: $\delta t = 4$ ns for the $CeBr_3$ and each of the eight BGO sections, $\delta t = 1$ ns for the EJ-200 and each of the two PMT in the SciFi detector. The timestamp of each event within a trace was calculated offline by performing a digital pole-zero cancellation followed by a Gaussian fit. Once the DAQ was triggered, the $N_{\mathrm{ch}} = 17$ channels were acquired simultaneously and therefore the relative ToF between two events in two channels was promptly calculated by subtracting the time of arrival of each event with respect to the start time of the trace. The absolute time of the events could also be obtained but it was not implemented since no synchronization with any external detector was required. The DAQ was used to acquire either the signals from the EJ-200 or the SciFi, i.e. we did not operate the two detectors simultaneously. The resulting data stream was approximately 2 kB/event, which converts to data sets of about 2 GB for a typical run with 10^6 raw events detected by the spectroscopic unit. In the collimated experiments we observed count rates up to $2 \cdot 10^3$ cps without dead time. In the uncollimated experiments we reached up to $4 \cdot 10^4$ cps with dead time below 10%.

The BGO signals were pre-amplified as described by Dal Bello et al., 2019. The high-voltage of the PMT coupled to the $CeBr_3$ was tuned to cover the $0.5 \div 10$ MeV gamma spectrum within the FADC dynamic range. The gain of the two PMT in the SciFi detector was also tuned to obtain the same signal amplitude at the two channels with a ^{90}Sr source during offline calibration runs.

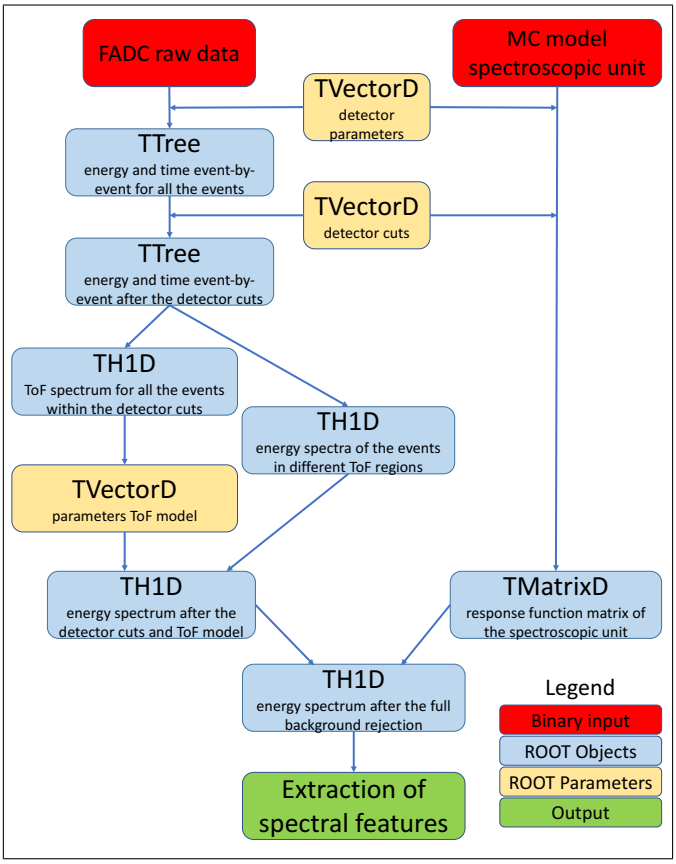

Figure 2. Overview of the workflow adopted to process the experimental data and obtain background-suppressed prompt gamma energy spectra. The different colors indicate the data format. The ROOT classes used to store the data are reported.

3. Data analysis and modelling

The experimental data was analyzed to extract the correlation between the prompt gamma spectra and the particles range. The current section presents the offline processes adopted to suppress the background and derive spectral features. Figure 2 presents an overview of the workflow, which individual steps are explained in detail in the following.

3.1. Response function of spectroscopic unit

The spectroscopic unit was characterized with the aim of improving its performance during the offline data analysis. The interactions of the high energy gamma radiation in the detectors were modeled to compute the response matrix of the system. The method was based on the results presented by Guttormsen et al., 1996, where the Compton continuum and the escape peaks are estimated in an iterative process and then subtracted from the measured spectra. The response matrix was generated with Monte Carlo (MC) radiation transport simulations using FLUKA, which is a general purpose MC software with applications in multiple fields (Ferrari et al., 2005) including

medical applications (Böhlen et al., 2014). We adopted the FLUKA version 2011.2x with the default settings `PRECISIOn`. The simulations included a full geometrical description of the $CeBr_3$ crystal, its envelope and the BGO crystals surrounding it.

The response matrix of the system was generated for incoming gamma with energy up to $E_\gamma = 10$ MeV. This covered the dynamic range of the experimental data defined by the detector parameters adopted in the first post-processing step represented in Figure 2. The pure energy deposition in the $CeBr_3$ (E_{dep}) was converted into the measured energy deposition (E_{mes}) by applying an energy spread according to the $CeBr_3$ resolution parameterized by Roemer et al., 2015, i.e. FWHM = 26.4 keV at $E_\gamma = 511$ keV. The events in coincidence with the surrounding BGO were removed to reproduce the same conditions as in the experimental setup. During this process, the energy resolution of the BGO was also taken into account, namely FWHM = 60.8 keV at $E_\gamma = 511$ keV. The values of the cuts applied to perform the anti-coincidence detection were shared with the routines used to process the experimental data in the second post-processing step of Figure 2. Then, we calculated the probability $P(E_{\text{mes}}, E_0)$ that such event had been generated by an incoming gamma ray with energy E_0. The matrix $P(E_{\text{mes}}, E_0)$ fully described the degradation of the prompt gamma spectrum due to the detection using the spectroscopic unit, the effect of the surrounding material was not modelled. Vertical projections of the matrix represented the response to mono-energetic radiation. Horizontal projections reported the probability distribution for the generation of a given measured energy.

3.2. Background rejection with detectors

The data was processed off-line using ROOT (Brun et al., 1997). The first background rejection was based on the data acquired by the primary and secondary detectors.

The spectroscopic unit was operated in anti-coincidence. We calibrated the energy deposition in the AC shield during a dedicated run with a ^{137}Cs source. Only in this case the DAQ was triggered by energy deposition in the BGO. The threshold for the anti-coincidence rejection was $E_\gamma = 50$ keV. When one of the BGO sections recorded an event above this threshold, the corresponding event in the $CeBr_3$ was a candidate to be discarded. The event was eventually removed if the two energy depositions happened within the anti-coincidence time window ($\Delta t = 25$ ns).

The beam trigger data was used to define a Time-of-Flight (ToF) window. Only the events that fell within the energy deposition cuts for the beam trigger were considered. The cuts were defined on the base of a Gaussian fit of the energy deposition for the heavy projectiles (^{12}C and ^{16}O) and a Landau fit for the light ones (p and ^{4}He). The data within the cuts included just part of the total distributions of the energy depositions; therefore, the correction factors for the fraction of the events left out of the analysis were also computed based on the Gaussian and Landau fits. Multiple ($\Delta t < 5$ ns) hits were discarded. Then, the time differences between the events in the $CeBr_3$ and the EJ-200 or the SciFi detector were computed. We set a ToF window of $\Delta t_{ToF} = 3$ ns for the

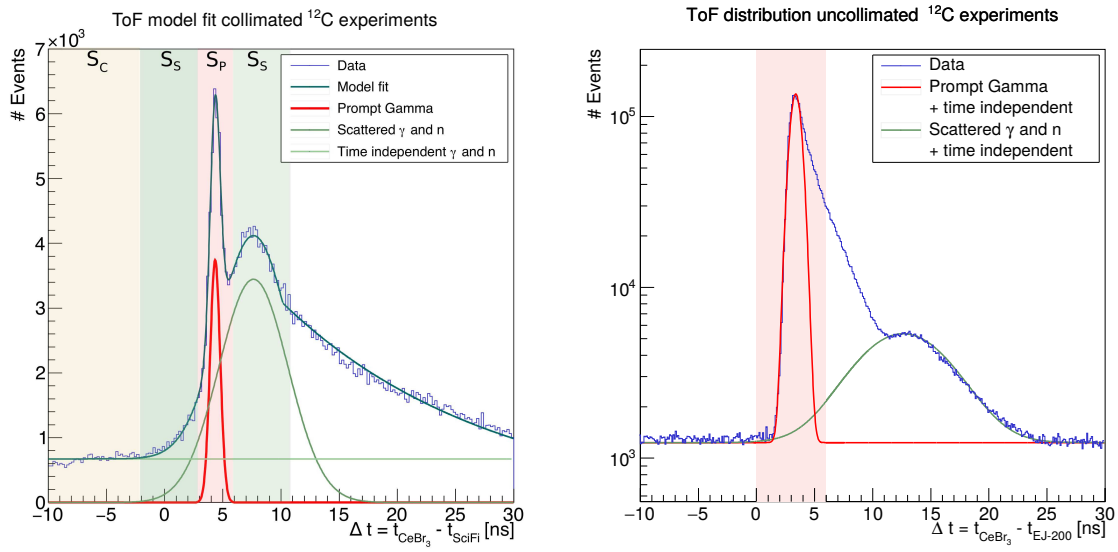

Figure 3. Left: Exemplary fit of the ToF model for data acquired in presence of the ^{12}C beam during the collimated experiments. The model and its individual components are plotted with different solid lines and are fitted to the data, which is presented as histogram. The highlighted areas represent the regions where the distributions S_P, S_S and S_C were sampled. Right: Example of ToF distribution obtained during the uncollimated experiments. Here, only the prompt and the scattered component are shown. The sampling of S_P is performed in the region where the prompt component is more intense than the scattered one.

experiments with the collimator and $\Delta t_{ToF} = 6$ ns for the ones without. These regions were the ones where the prompt gamma events were more intense than the scattered events, as shown in Figure 3. The events in the $CeBr_3$ within these time windows were accepted to define the prompt gamma energy spectrum S_P. The events outside the cuts were also stored for further processing. In particular, we defined two time windows (each $\Delta t_S = 5$ ns) to sample the energy spectrum of the scattered radiation S_S before and after the prompt gamma peak. A wide time window ($\Delta t_C = 45$ ns) was also defined before the previous ToF cuts to sample the energy spectrum S_C of the time independent radiation. A graphic representation of the ToF regions where S_P, S_S and S_C were sampled is presented in Figure 3.

Finally, the first calibration of the energy deposition in the $CeBr_3$ was based on the ^{137}Cs source by selecting the events acquired during beam-on conditions, but outside the ToF cuts. Non-linearity effects were not taken into account at this stage.

3.3. Background rejection with models

The background rejection was refined with dedicated models.

First, the ToF spectra was modelled. The identification of its different components during ion irradiation was investigated by Testa et al., 2010. We based our modelling on this previous study and we defined the following ToF distributions: $f_P(t)$ as the prompt

gamma events; $f_S(t)$ as the scattered gamma or the gamma produced in (n,γ) reactions; $f_A(t)$ as the events associated with activation having a characteristic decay time shorter than the time between bunches and $f_C(t)$ as the time independent component, i.e. generated by activation with decay time longer than the time between bunches. The first two components were mainly made up by discrete emission lines. On the other hand, the second two contained mainly a continuum background and the most prominent discrete peaks were the one at $E_\gamma = 0.511$ MeV following the β^+ decays and the one at $E_\gamma = 2.22$ MeV from the hydrogen neutron capture.

The total ToF spectrum was then parametrized by:

$$f_{ToF}(t) = f_P(t) + f_S(t) + f_A(t) + f_C(t) \tag{1}$$

where $f_P(t) = \mathcal{N}(\mu_P, \sigma_P)$ and $f_S(t) = \mathcal{N}(\mu_S, \sigma_S)$ were modelled by Gaussian functions, $f_A(t) = \theta(t - \mu_S - \sigma_S) \cdot e^{-\tau_A \cdot t}$ by an exponential function and $f_C(t)$ by a constant. We set the conditions: $\mu_P < \mu_S$ and $\sigma_P < \sigma_S$. In a following step, we fitted the ToF spectra with (1) and defined the following quantities: the correction factor for the prompt gamma ToF cut

$$k_P = \left(\int_{\mu_P - 0.5\cdot\Delta t_{ToF}}^{\mu_P + 0.5\cdot\Delta t_{ToF}} f_P(t) \cdot \mathrm{d}t \right) \cdot \left(\int_{-\infty}^{+\infty} f_P(t) \cdot \mathrm{d}t \right)^{-1} \tag{2}$$

and the correction factor for the scattered or (n,γ) events in the ToF cut

$$k_S = \left(\int_{\mu_P - 0.5\cdot\Delta t_{ToF}}^{\mu_P + 0.5\cdot\Delta t_{ToF}} f_S(t) \cdot \mathrm{d}t \right) \cdot \left(\int_{\mu_P - 0.5\cdot\Delta t_{ToF} - \Delta t_S}^{\mu_P - 0.5\cdot\Delta t_{ToF}} f_S(t) \cdot \mathrm{d}t + \int_{\mu_P + 0.5\cdot\Delta t_{ToF}}^{\mu_P + 0.5\cdot\Delta t_{ToF} + \Delta t_S} f_S(t) \cdot \mathrm{d}t \right)^{-1}. \tag{3}$$

This model and its parameters were adopted to further process the experimental data. The spectrum S_C was scaled once by the factor $2 \cdot \Delta t_S / \Delta t_C$ and once by $\Delta t_{ToF} / \Delta t_C$ to subtract it from S_S and S_P, respectively, obtaining $S_{S,\mathrm{no}C}$ and $S_{P,\mathrm{no}C}$. The $S_{S,\mathrm{no}C}$ was scaled by the factor k_S calculated in (3) and subtracted from $S_{P,\mathrm{no}C}$. Finally, this result was scaled by the factor k_P^{-1} calculated in (2). The component $f_A(t)$ was neglected as its contribution was negligible in the ToF cut for prompt gamma.

Then, we employed the response function calculated in section 3.1. The matrix $P(E_{\mathrm{mes}}, E_0)$ was used to unfold the experimental data according to the method described by Guttormsen et al., 1996. Such method has also been successfully applied in a previous prompt gamma study by Vanstalle et al., 2017.

Finally, the non-linearity effects in the energy calibration were corrected. To do so, we used the known position of the high energy spectral line and refined the first energy calibration performed with the ^{137}Cs source. Such fine tuning contributed $< 5\%$ to the overall calibration.

4. Experimental campaigns

Several experimental campaigns have been performed. The experiments shared the same detectors, data acquisition system and post-processing routines. The experiment-

specific features are presented in the current section.

4.1. Ion beam characteristics

The experiments were conducted at the Heidelberg Ion-Beam Therapy Center (HIT), Heidelberg, Germany (Haberer et al., 2004). Beams of p, ^{4}He, ^{12}C and ^{16}O were delivered to the experimental cave. The active feedback system was activated to guarantee the stability of the parameters and we adopted beam energies and intensities available in the therapy control system (TCS)‡. The nominal beam intensities varied from a minimum of $5{\cdot}10^{6}$ ions$\cdot$s^{-1} for ^{16}O beams to a maximum of $8{\cdot}10^{7}$ ions$\cdot$s^{-1} for p beams. The intervals between the bunches ranged from approximately 150 ns to 350 ns and the bunch widths from 20 ns to 75 ns. The SciFi detector was used to measure the arrival time of the single particles within the bunches, as demonstrated by Magalhaes Martins et al., 2019. During all the experimental campaigns the beam was delivered at the isocenter at a fixed energy for each run. The energies for the collimated experiments were chosen to position the Bragg peak at a depth of $z = (87.0 \pm 0.3)$ mm in the water phantom for all the ion beams. Moreover, the nominal beam intensity refers to one during beam-on condition and the ratio spill to inter-spill time was approximately $1 : 1$.

4.2. Targets

Four different targets have been used during the experiments:

(i) The *PMMA target*. It consisted of four Polymethyl-methacrylate blocks of size $25 \times 25 \times 5$ cm^3. We aligned the blocks to obtain a thickness of $l = 20$ cm of PMMA in the beam direction. In first approximation, this phantom is equivalent to a uniform PMMA block.

(ii) The *Water phantom*. This target can be seen at the center of the experimental setup in Figure 1. The phantom was the MP3-P water tank produced by PTW§. We filled it with approximately $V = 15$ l of double distilled water and we oriented it with the thin ($l = 5$ mm) beam entrance window facing the nozzle. The water phantom was placed on a moving platform, which allowed movements in two directions with a step size of $\Delta l = 10$ μm.

(iii) The *Water target*. It consisted of five flasks filled with double distilled water and aligned to the beam direction. The total water thickness in beam direction was $l = 16$ cm, while the total thickness of the polystyrene flasks walls was $l = 0.9$ cm. In first approximation, this phantom is equivalent to a uniform water cube with regular inserts of thin polystyrene orthogonal to the beam direction.

(iv) The *Water+Ti target*. This was obtained placing a titanium slab of thickness $l = 0.6$ cm between the third and the fourth flask of the water target.

‡ Siemens Healthcare GmbH, Erlangen, Germany
§ Physikalisch-Technische Werkstätten GmbH, Freiburg, Germany

Collimated experiment (Water phantom)

Ion	E [MeV/u]	N_0/ position	# positions
p	108.88	$9.6 \cdot 10^{10}$	2
^{4}He	109.97	$3 \cdot 10^{10}$	2
^{12}C	204.27	$8 \cdot 10^{9}$	20
^{16}O	241.0	$5 \cdot 10^{9}$	2

Uncollimated experiments

Ion	E [MeV/u]	N_0 (PMMA target)	N_0 (Water target)	N_0 (Water+Ti target)
p	148.21	$6 \cdot 10^{10}$	$8.6 \cdot 10^{10}$	$7.6 \cdot 10^{10}$
^{4}He	149.02	$1.5 \cdot 10^{10}$	$1.4 \cdot 10^{10}$	$1.2 \cdot 10^{10}$
^{12}C	281.57	$3.4 \cdot 10^{9}$	$5 \cdot 10^{9}$	$1 \cdot 10^{10}$
^{16}O	333.91	-	$1.2 \cdot 10^{9}$	$1.9 \cdot 10^{9}$

Table 1. Breakdown of the experiments conducted at HIT. The number of ions irradiated, their type and energy associated to each experimental setup and target are reported. The blank entry corresponds to one experiment that was not performed.

The phantom (ii) had an internal rail for precise positioning of an ionization chamber support. We customized the support to hold a Gafchromic EBT3 film‖, which we used to verify the range of the primary particles in the water phantom. The range measurement took into account the presence of the beam trigger and was estimated to have precision of $\sigma = 0.3$ mm. The under-response of the EBT3 film was approximated as a constant from the maximum of the dose deposition to its 80% value (Castriconi et al., 2017).

4.3. Uncollimated experiment: reactions identification

The first set of experiments aimed to identify the nuclear de-excitation channels observable with our system. Therefore, we did not introduce any collimator in the experimental setup and we measured the prompt gamma emission over the full target aiming to maximize the statistics. The experimental setup was analogous to the one used in Dal Bello et al., 2019. The spectroscopic unit was placed at $d = 10$ cm from the beam axis and we acquired approximately $N_{\text{ev}} = 2 \cdot 10^7$ raw events in the spectroscopic unit for each run. The beam trigger was the EJ-200. The irradiated targets and the corresponding properties of the ion beams are reported in Table 1. The data was post-processed according to the methods presented in section 3. The final results, i.e. the background-suppressed spectra, were used to identify the discrete prompt gamma lines generated during the irradiation. Moreover, we fitted the width of the spectral lines in the water target experiment and we quantified the relation between their FWHM and the mass of the projectile. The theoretical derivation of the functional form used in the

‖ Ashland Inc., Ashland, U.S.

fitting is developed in the dedicated appendix section A.

4.4. Collimated experiment: Bragg peak position

The second set of experiments aimed to correlate the intensity of the spectral lines identified in the uncollimated experiments to the position of the Bragg peak. Therefore, a tungsten slit collimator was introduced in the setup, as shown in Figure 1. The collimator was $t = 12.5$ cm thick, it had a vertical opening of $s = 7.5$ mm and it was placed at $d = (20.0 \pm 0.1)$ cm from the beamline. The principal axis of the spectroscopic unit was aligned with the center of the slit collimator and the target taking as reference point the depth of 9 cm in the water phantom. This was done using the laser positioning system available at the experimental cave, obtaining an alignment with an estimated precision below the millimeter. The frontal face of the $CeBr_3$ was positioned at $d = (40.0 \pm 0.1)$ cm from the beamline.The beam trigger was the SciFi.. We selected the same energy step in the TCS for the four ions in order to generate the Bragg peak always at the same depth in the water phantom, namely at $z = (87.0 \pm 0.3)$ mm from the beam entrance window, which was verified with the Gafchromic EBT3 films. The relative longitudinal position z between the water phantom and the spectroscopic unit was varied operating the moving platform and therefore the prompt gamma radiation was measured at different depths in the phantom. The moving platform was operated with multiple incremental steps of $\Delta z = 10$ μm each. For each of the p, ^{4}He and ^{16}O beams we acquired one data set before the Bragg peak ($z = 80$ mm) and one after it ($z = 105$ mm). For the ^{12}C beam we acquired 20 positions along the phantom from $z = 25$ mm to $z = 120$ mm with a spacing of $\Delta z = 5$ mm. Each measurement point comprised of exactly 200 spills of 5 seconds beam-on each. This resulted in data sets of approximately $N_{\mathrm{ev}} = 10^6$ raw events in the spectroscopic unit. The summary of the beam characteristics is reported in Table 1. The data was post-processed according to the methods presented in section 3. Further data analysis was conducted for the collimated experiments.

First, we compared the ToF spectra between the $CeBr_3$ and the SciFi detector before ($z = 80$ mm) and after ($z = 105$ mm) the Bragg peak. For all the four ions the events with energy deposition in the $CeBr_3$ between $E_\gamma \geq 0.6$ MeV and $E_\gamma \leq 6.8$ MeV were chosen. We identified and fitted the widths of the primary peaks in the ToF distributions for $z = 80$ mm.

Then, we compared the background-suppressed energy spectra detected by the spectroscopic unit before ($z = 80$ mm) and after ($z = 105$ mm) the Bragg peak. The high-frequency noise was suppressed applying a smoothing proportional to the intrinsic energy resolution of the $CeBr_3$ (Roemer et al., 2015). For the ^{12}C or ^{16}O beams the analysis included both the prompt gamma emission of the target and the projectile nuclei. In particular, for the ^{12}C projectile the Doppler shift of the $E_\gamma = 4.4$ MeV line and for the ^{16}O of the $E_\gamma = 6.1$ MeV line were analyzed. The theoretical derivation of the Doppler shifts at $z = 80$ mm is presented in the dedicated appendix section A.

Finally, we analyzed the evolution of the intensity of the spectral lines with respect to the Bragg peak position in presence of the ^{12}C beam. At every z_i position of the water phantom, we integrated the counts of the discrete peaks over the energy interval $E_0 \pm 3 \cdot \sigma_0$. Here, the analysis was limited to the prompt gamma emitted by the de-excitation of the target nuclei and therefore the values E_0 were fixed and not corrected according to the Doppler effect. The number of prompt gamma was calculated by adding the events in the relevant histogram bins. Such counting process was chosen over a more complex fit routine to minimize the free parameters in the current proof-of-concept study. The fitting routine should be preferred when an accurate determination of the absolute counts is required. E_0 was the nominal energy of the discrete peak and σ_0 was the nominal peak width calculated from the $CeBr_3$ intrinsic energy resolution. We also measured the full prompt gamma emission integrated from $E_\gamma = 0.6$ MeV to $E_\gamma = 6.8$ MeV. The number of events within the integration window was used to calculate the uncertainties according to the Poisson statistics ($\sigma_I = \sqrt{N_\gamma}$). Then, the counts were normalized by the number of irradiated ^{12}C ions and the corresponding correction factors to take into account the cuts in the energy deposition distribution in the trigger previously calculated were applied, obtaining $I_j(z_i)$ at every position i and for each gamma line j. To better visualize the evolution of the intensities with the position in the water phantom we superimposed the data with a smoothed curve. Such curve was obtained with the dedicated function `SmoothLowess` in the `TGraphSmooth` class of ROOT (Brun et al., 1997). The smoothing factor was $f = 1/5$ and the standard deviation of the smoothed values from the data points was also calculated, which was then plotted as a band about the smoothed curve. We concluded the analysis by computing the ratio of the intensities of five pairs of independent spectral lines at every z_i and propagating the statistic uncertainties. The ratios of the intensities $R_{j,k}(z_i) = I_j(z_i)/I_k(z_i)$ were parametrized with a third degree polynomials in the neighborhood of the Bragg peak. The aim was to investigate whether it exists a set of monotonic and therefore invertible functions that correlate the absolute range of the primary particles to the detected spectral features. The existence of such relations would demonstrate the possibility to perform the opposite process, i.e. using the prompt gamma energy spectra to recover the absolute range of the primary ^{12}C ions. The functional forms describing $R_{j,k}(z_i)$ depend on the attenuation of the prompt gamma in the target, its elemental composition and the detector setup. The parameterization of such phenomena will be required for absolute range verification during patient treatment. In this work, we fixed these parameters to determine the existence of invertible functions in an exemplary situation.

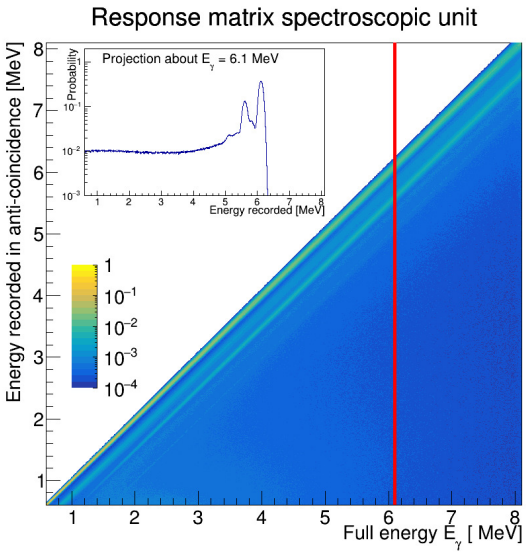

Figure 4. Response function matrix for the spectroscopic unit. The logarithmic color scale reports the probability to obtain the corresponding energy deposition. The vertical line indicates the response to a monoenergetic photon beam of $E_\gamma = 6.1$ MeV. The insert shows the simulation of its corresponding energy spectrum.

5. Results

The results of this study include the performances of the post processing routines and the extraction of spectral features, eventually correlating the prompt gamma yield to the range of the ions in the target. The current section presents the results from the experimental campaigns.

5.1. Response function of spectroscopic unit

The response function of the spectroscopic unit is presented in Figure 4. The matrix maps the probability of obtaining a specific energy deposition in the spectroscopic unit operated in anti-coincidence given the energy of the incoming gamma radiation. The insert in Figure 4 shows the Monte Carlo simulated energy spectrum obtained with an incoming $E_\gamma = 6.1$ MeV gamma. It can be observed that the detection of the photo peak is promoted with respect to the background components. The ratio between the events in the photo peak and the ones in the single escape peak was 2.4, while the amplitude of the Compton continuum component was about a factor 30 smaller than the photo peak. The matrix generated with Monte Carlo and presented in Figure 4 was used in the following steps to improve the background rejection.

5.2. Background rejection

5.2.1. Time-of-Flight model An example of a ToF spectrum and the corresponding fit of the model described by equation (1) is shown in Figure 3. The data presented was

obtained in the collimated experiments in presence of ^{12}C beams. It can be seen how the $f_P(t)$ and the $f_S(t)$ components can be separated with the time resolution of the system. In this specific case, the time separation was $\Delta t_{P,S} = \mu_S - \mu_P = 3.3$ ns. In Figure 3 we observed a factor $\times 6.4$ more events in the $f_S(t)$ peak compared to the $f_P(t)$ peak. These events were subtracted according to the method presented in section 3.3. The events in the time independent component $f_C(t)$ had a smaller contribution within the ToF cuts; nonetheless, we processed and subtracted them. On the other hand, the fast decaying events $f_A(t)$ had a negligible contribution to the prompt gamma peak. Therefore, we fitted their ToF distribution but we did not process such events further. A similar behaviour was observed also in the other data sets with different target and in presence of distinct ion beams. It should be noticed that in the uncollimated experiments and in presence of lighter ion beams the width of the $f_P(t)$ distribution increased. The quantitative analysis of such effect is presented in a following paragraph.

5.2.2. Full background rejection An example of all the progressive steps undertaken to obtain the background-suppressed spectra is shown in Figure 5. The raw data without any cut was omitted. It can be observed how the background component is progressively subtracted from the data until obtaining a spectrum mainly composed by the discrete lines. To analyze the contribution of each step, we assumed as the 100% reference the entries in the energy spectra in the range $E_\gamma \in (0.6 \div 6.8)$ MeV after the ToF window. We observed that by applying the anti-coincidence detection with the BGO the number of events accepted decreased to 45.5%. The application of the ToF model improves the signal to noise ratio especially at the low energy component of the spectrum and suppressed the hydrogen neutron capture line. As a matter of fact, a local minimum was observed at $E_\gamma = 2.2$ MeV in Figure 5 after the ToF model. The fraction of events left after this step was 12.7%. Finally, the unfolding of the spectrum further removes the detector contributions such as the Compton continuum and the escape peaks. The background-suppressed spectrum contains 8.3% of the initial events. This final drop has to be attributed to events identified as part of the Compton continuum in the range $E_\gamma \in (0.6 \div 6.8)$ MeV, which during the unfolding were pushed to the region $E_\gamma > 6.8$ MeV and therefore not further processed. Analogous fractions of removed events were observed for other beam species in the steps introducing the anti-coincidence detection and the unfolding of the spectrum. The number of events removed by the ToF model depended on the beam type and increased with increasing mass of the projectile.

5.3. Reactions identification

The background-suppressed spectra acquired during the uncollimated experiments are presented in Figure 6. We identified 19 independent spectral lines in the three targets irradiated. The complete list of the reactions observed for every beam species are reported in Table 2.

The quantitative analysis of the evolution of the width of the spectral lines for the

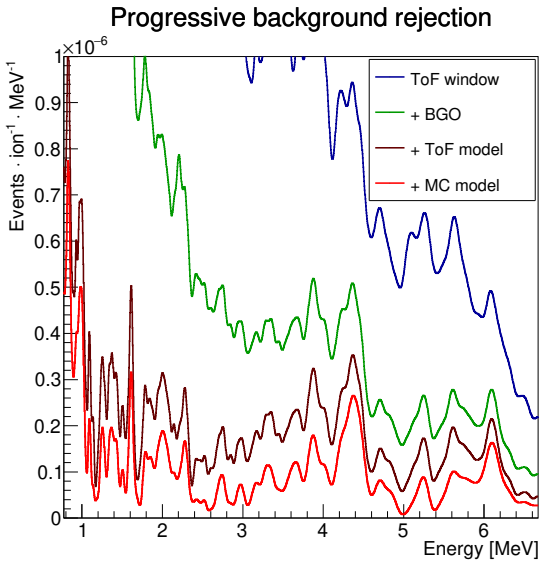

Figure 5. Progressive steps in background rejection. The solid lines show the obtained spectra after the cumulative introduction of each step in the post processing. The data was acquired in presence of the ^{12}C beam during the collimated experiments. The collimator slit was aligned to the Bragg peak location in the water phantom.

water target with increasing mass of the projectile is shown in Figure 7. We selected the most and the least energetic prompt gamma listed in Table 2. It can be observed how the model (13) derived in Appendix A correctly reproduces the experimental data. We observed positive deviations of the FWHM with respect to the intrinsic $CeBr_3$ resolution reported by Roemer et al., 2015. The minimum deviation was observed in presence of p beams for the $E_\gamma = 0.718$ MeV line, namely a factor $\times 1.22$ wider. The maximum deviation was observed in presence of ^{16}O beams for the $E_\gamma = 6.1$ MeV line, namely a factor $\times 2.97$ wider. The average increase of the FWHM was $\times 1.51$ for the $E_\gamma = 0.718$ MeV line and $\times 2.55$ for the $E_\gamma = 6.1$ MeV line. It should be reminded that the FWHM values in Roemer et al., 2015 have been calculated with negligible Doppler broadening, i.e. using sources or low energetic p beams.

5.4. ToF spectra and Bragg peak position

The collimated experiments presented different features for the data sets acquired before and after the Bragg peak position. Figure 8 shows the ToF spectra between the $CeBr_3$ and the SciFi detector signals. The count rates are reported in events per primary ion per nanosecond. For all the four ion beam species we observed differences between $z = 80$ mm and $z = 105$ mm. In particular, for the p and ^{4}He beams, the events in the prompt gamma peak were observable predominantly in the data acquired upstream the Bragg peak and they were comparable with the background downstream to it. On the other hand, for the ^{12}C and ^{16}O beams, such events were observable in both the positions with different intensities. In this case the ratio of the maximum instantaneous

			Reactions induced by:			
E_γ [MeV]	Target nuclei	De-excitation reactions	p	^{4}He	^{12}C	^{16}O
6.1	^{16}O ^{16}O	$^{16}O^*_{6.13} \rightarrow {}^{16}O_{g.s.}$ $^{15}O^*_{6.18} \rightarrow {}^{15}O_{g.s.}$	✓	✓	✓	✓
5.2	^{16}O ^{16}O ^{16}O ^{16}O	$^{15}O^*_{5.18} \rightarrow {}^{15}O_{g.s.}$ $^{15}O^*_{5.24} \rightarrow {}^{15}O_{g.s.}$ $^{15}N^*_{5.27} \rightarrow {}^{15}N_{g.s.}$ $^{15}N^*_{5.30} \rightarrow {}^{15}N_{g.s.}$	✓	✓	✓	✓
4.4	^{16}O ^{16}O ^{12}C ^{12}C	$^{12}C^*_{4.44} \rightarrow {}^{12}C_{g.s.}$ $^{11}B^*_{4.45} \rightarrow {}^{11}B_{g.s.}$ $^{12}C^*_{4.44} \rightarrow {}^{12}C_{g.s.}$ $^{11}B^*_{4.45} \rightarrow {}^{11}B_{g.s.}$	✓	✓	✓	✓
3.68	^{16}O ^{12}C	$^{13}C^*_{3.68} \rightarrow {}^{13}C_{g.s.}$ $^{13}C^*_{3.68} \rightarrow {}^{13}C_{g.s.}$	×	✓	✓	✓
3.21	^{16}O ^{12}C	$^{12}C^*_{7.65} \rightarrow {}^{12}C^*_{4.44}$ $^{12}C^*_{7.65} \rightarrow {}^{12}C^*_{4.44}$	×	✓	✓	✓
2.7	^{16}O ^{16}O ^{16}O ^{16}O ^{12}C ^{12}C	$^{16}O^*_{8.87} \rightarrow {}^{16}O^*_{6.13}$ $^{14}N^*_{5.11} \rightarrow {}^{14}N^*_{2.31}$ $^{11}C^*_{4.80} \rightarrow {}^{11}C^*_{2.00}$ $^{10}B^*_{3.59} \rightarrow {}^{11}B^*_{0.718}$ $^{11}C^*_{4.80} \rightarrow {}^{11}C^*_{2.00}$ $^{10}B^*_{3.59} \rightarrow {}^{10}B^*_{0.718}$	✓	✓	✓	✓
2.31	^{16}O	$^{14}N^*_{2.31} \rightarrow {}^{14}N_{g.s.}$	✓	✓	✓	✓
2.12	^{12}C	$^{11}B^*_{2.12} \rightarrow {}^{11}B_{g.s.}$	✓	✓	✓	n.a.
2.0	^{16}O ^{16}O ^{12}C	$^{11}C^*_{2.00} \rightarrow {}^{11}C_{g.s.}$ $^{15}O^*_{7.28} \rightarrow {}^{15}O^*_{5.24}$ $^{11}C^*_{2.00} \rightarrow {}^{11}C_{g.s.}$	✓	✓	✓	✓
1.88	^{16}O ^{12}C	$^{15}N^*_{7.16} \rightarrow {}^{15}N^*_{5.27}$ $^{15}N^*_{7.16} \rightarrow {}^{15}N^*_{5.27}$	✓*	✓	✓	✓
1.64	^{16}O ^{12}C	$^{14}N^*_{3.95} \rightarrow {}^{14}N^*_{2.31}$ $^{14}N^*_{3.95} \rightarrow {}^{14}N^*_{2.31}$	✓	✓	✓	✓
1.38	^{16}O ^{12}C	$^{15}O^*_{7.56} \rightarrow {}^{15}O^*_{6.18}$ $^{15}O^*_{7.56} \rightarrow {}^{15}O^*_{6.18}$	✓*	✓	✓	✓
1.3	^{48}Ti	$^{46}Ti^*_{3.29} \rightarrow {}^{46}Ti^*_{2.01}$ $^{47}Ti^*_{1.44} \rightarrow {}^{47}Ti^*_{0.159}$ $^{48}Ti^*_{2.29} \rightarrow {}^{48}Ti^*_{0.983}$	✓	✓	✓	✓
1.1	^{48}Ti	$^{46}Ti^*_{2.01} \rightarrow {}^{46}Ti^*_{0.889}$ $^{47}Ti^*_{1.25} \rightarrow {}^{47}Ti^*_{0.159}$	✓	✓	✓	✓
1.02	^{16}O ^{12}C	$^{10}B^*_{1.74} \rightarrow {}^{10}B^*_{0.718}$ $^{10}B^*_{1.74} \rightarrow {}^{10}B^*_{0.718}$	✓	✓	✓	×
0.937	^{16}O	$^{18}F^*_{0.937} \rightarrow {}^{18}F_{g.s.}$	×	×	✓	✓
0.983	^{48}Ti	$^{48}Ti^*_{0.938} \rightarrow {}^{48}Ti_{g.s.}$	✓	✓	✓	✓
0.889	^{48}Ti	$^{46}Ti^*_{0.889} \rightarrow {}^{46}Ti_{g.s.}$	✓	✓	✓	✓
0.718	^{16}O ^{12}C	$^{10}B^*_{0.718} \rightarrow {}^{10}B_{g.s.}$ $^{10}B^*_{0.718} \rightarrow {}^{10}B_{g.s.}$	✓	✓	✓	✓

Table 2. List of reactions observed during the uncollimated experiments. Multiple de-excitation reactions, which were merged in the experimental data, are reported in a common row. For each projectile, we indicated with (✓) the observed spectral lines and with (×) the reactions that were not observable or that had a negligible intensity. For the p beams, some reactions were observed only on ^{16}O target (✓*). For the ^{16}O beams, the data on ^{12}C targets is missing and one entry was not assigned (n.a.). The de-excitation reactions were retrieved from the NUDAT database (Kinsey, 1998).

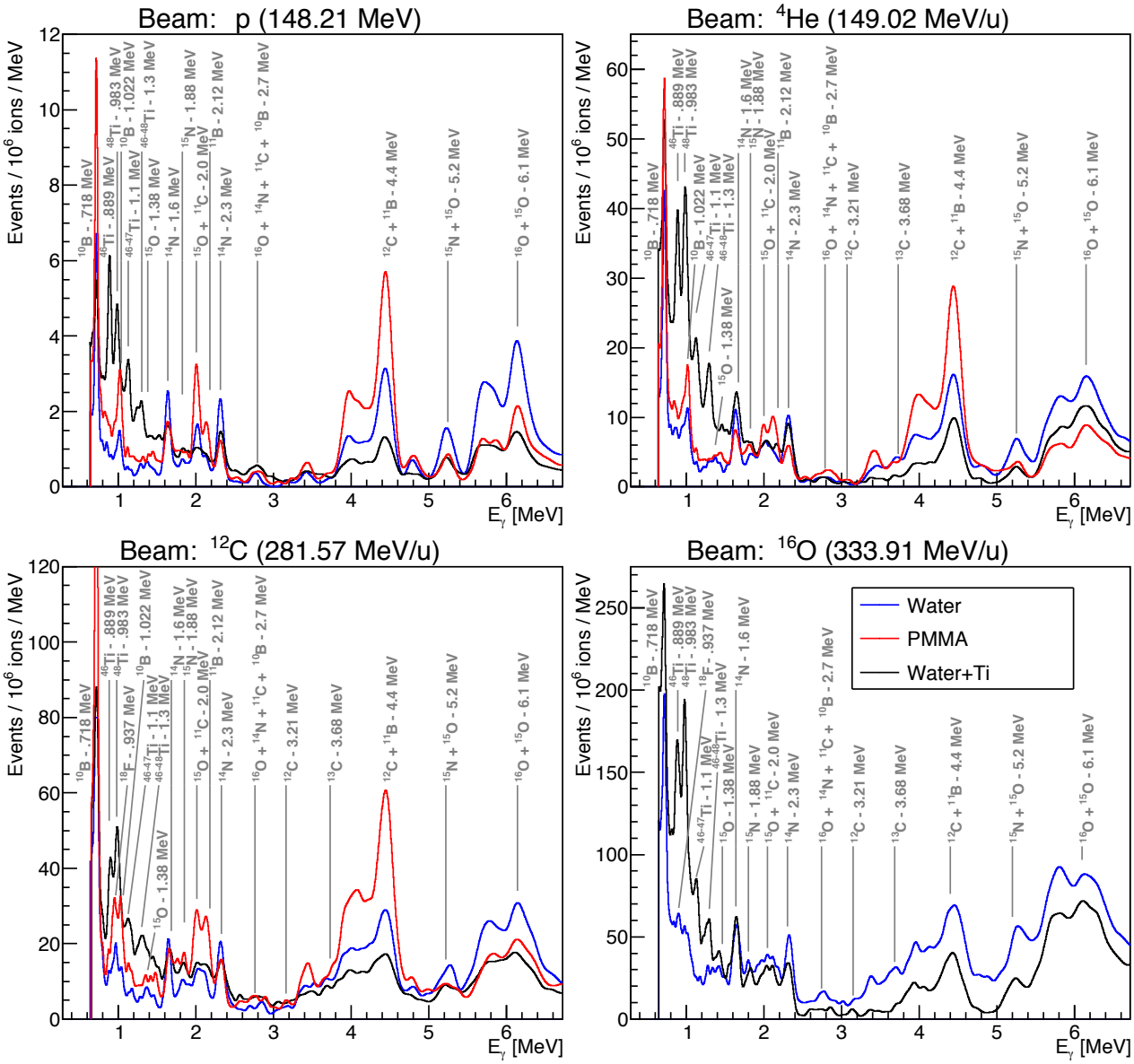

Figure 6. Background-suppressed spectra and identification of the reaction channels for the uncollimated experiments. The vertical lines indicate the position of the identified peaks. The labels report the nominal energy of the gamma line and the nuclei undergoing the de-excitation. The data was smoothed for better visualisation.

count rates between $z = 80$ mm and $z = 105$ mm was approximately 2 and their values downstream the Bragg peak were compatible with the ones observed for the scattered events. Moreover, we observed that the count rates at $\Delta t = 25$ ns converged to the same values for ^{4}He, ^{12}C and ^{16}O beams, while for p beams we measured an event rate + 13% higher for $z = 80$ mm compared to $z = 105$ mm. Finally, we observed a sharper ToF peak for the prompt gamma events generated by heavier projectiles, down to FWHM = 1.08 ns for ^{16}O beams. The values of the standard deviations of the primary prompt gamma peaks are reported in Figure 8. As a consequence, the ratio

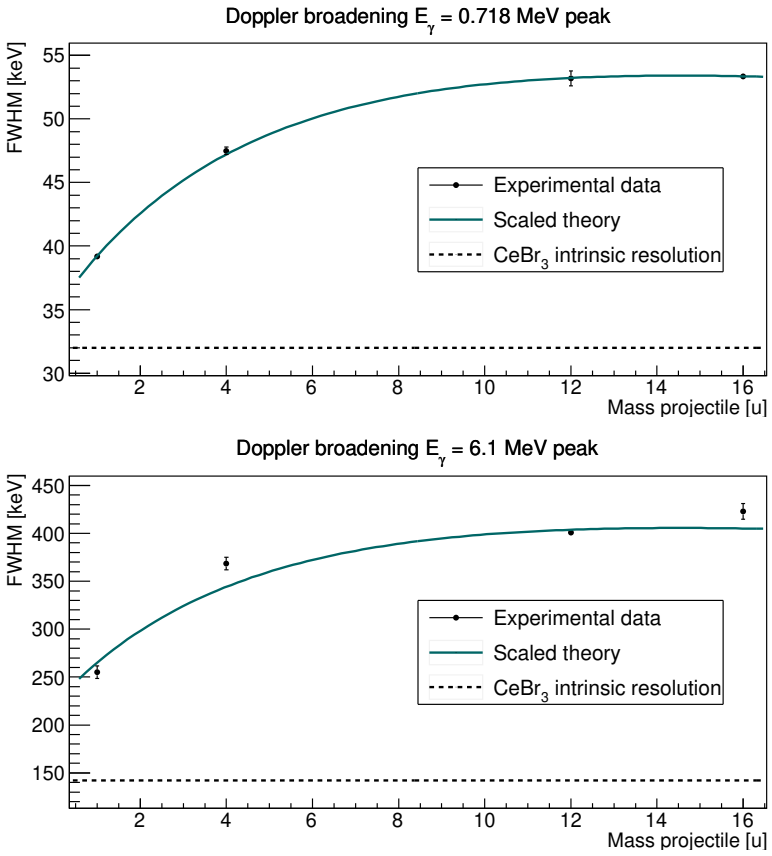

Figure 7. Evolution of the spectral lines FWHM with increasing projectile mass. The bullets report the experimental data with the water target from the uncollimated experiments. The solid line was calculated from equation (13) scaling κ. The dashed line is the nominal $CeBr_3$ resolution calculated according to Roemer et al., 2015.

between the maximum and the minimum count rate strongly depended on the projectile. For p, ^{4}He, ^{12}C and ^{16}O the ratios were respectively: $r = 1.8$, $r = 2.1$, $r = 8.8$ and $r = 14.2$.

5.5. Energy spectra and Bragg peak position

5.5.1. Binary position The most significant differences between the data acquired upstream and downstream the Bragg peak were observable in the energy spectra reported in Figure 9. A drop of the intensities of the discrete lines was observed when moving from $z = 80$ mm to $z = 105$ mm, both for the high and for the low energy part of the spectra. In particular, we report that for p beams the most energetic lines ($E_\gamma \geq 4.4$ MeV) were not observable at the position downstream the Bragg peak. On the other hand, for heavier projectiles the intensity of such lines were strongly reduced but the peaks in the energy spectra were still identifiable. The gamma lines at lower energy could be observed both upstream and downstream the Bragg peak with different intensities. The number of total events detected in the energy window $0.6 \div 6.8$ MeV

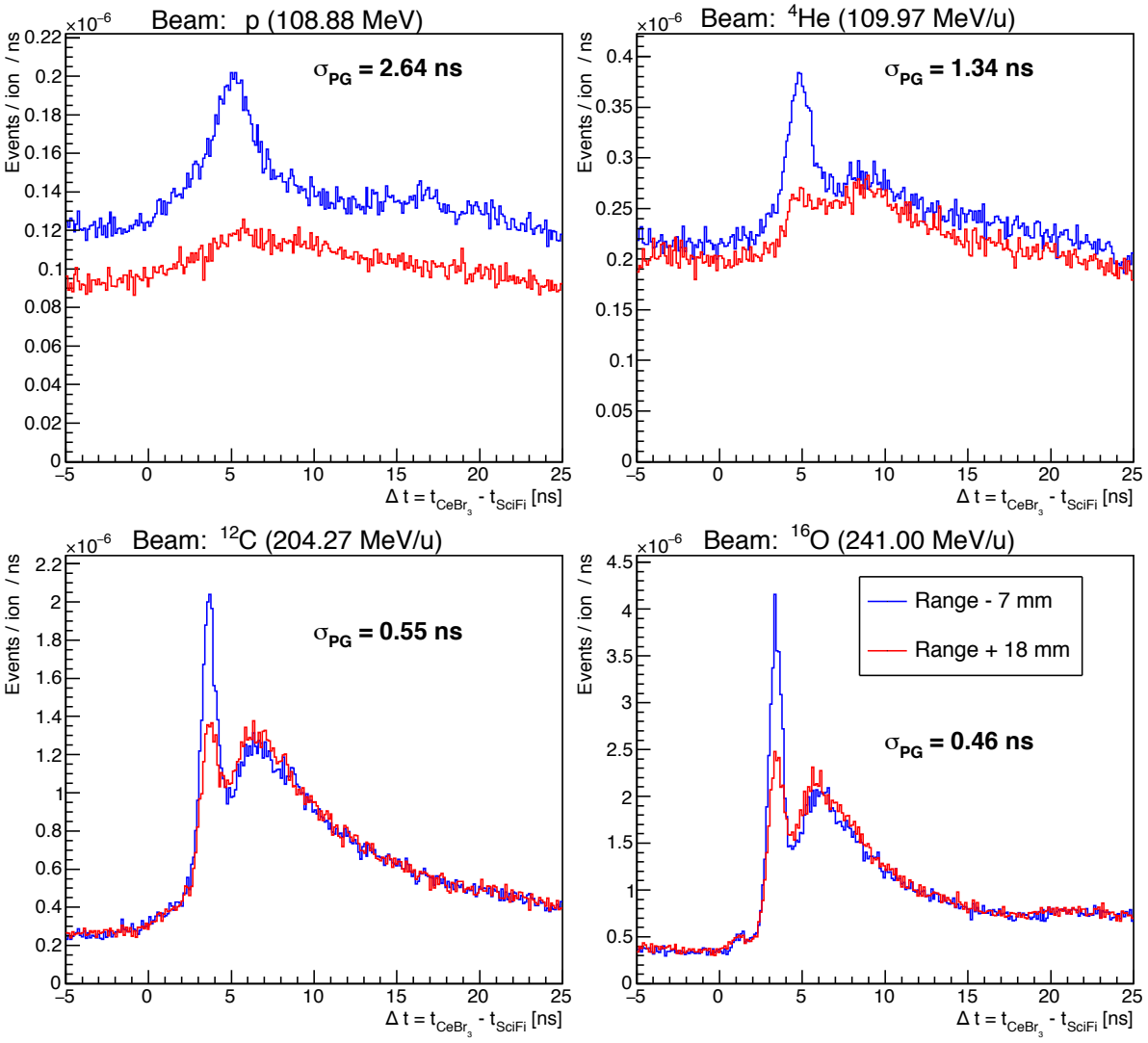

Figure 8. Time-of-Flight spectra for the prompt gamma radiation before and after the Bragg peak obtained in the collimated experiments. The comparison between the four ion species is shown. The labels in the plots report the widths of the prompt gamma peaks upstream the Bragg peak, i.e. the fit performed on the blue histogram. The counts are integrated over the $0.6 \div 6.8$ MeV energy range.

normalized per primary ion depended on the mass of the projectile. We considered the spectra acquired at $z = 80$ mm and we compared the number of events taking the ^{12}C data as the reference. For p and ^{4}He beams we measured factors of $\Gamma_{^{12}C,^{1}p} = 7.8$ and $\Gamma_{^{12}C,^{4}He} = 4.8$ less events, respectively. For ^{16}O we measured a factor $1/\Gamma_{^{12}C,^{16}O} = 2.1$ more events.

One further effect was observed in presence of ^{12}C and ^{16}O beams. Additionally to the discrete lines identified in Figure 6, one more peak was detected in each spectrum in Figure 9 at $z = 80$ mm. Namely, we identified a peak at $E_\gamma = 4.2$ MeV for the ^{12}C data and a peak at $E_\gamma = 5.8$ MeV for the ^{16}O data. Such lines were not observable at $z = 105$ mm. We calculated in Appendix A the Doppler shifts of the $E_\gamma = 4.4$ MeV and

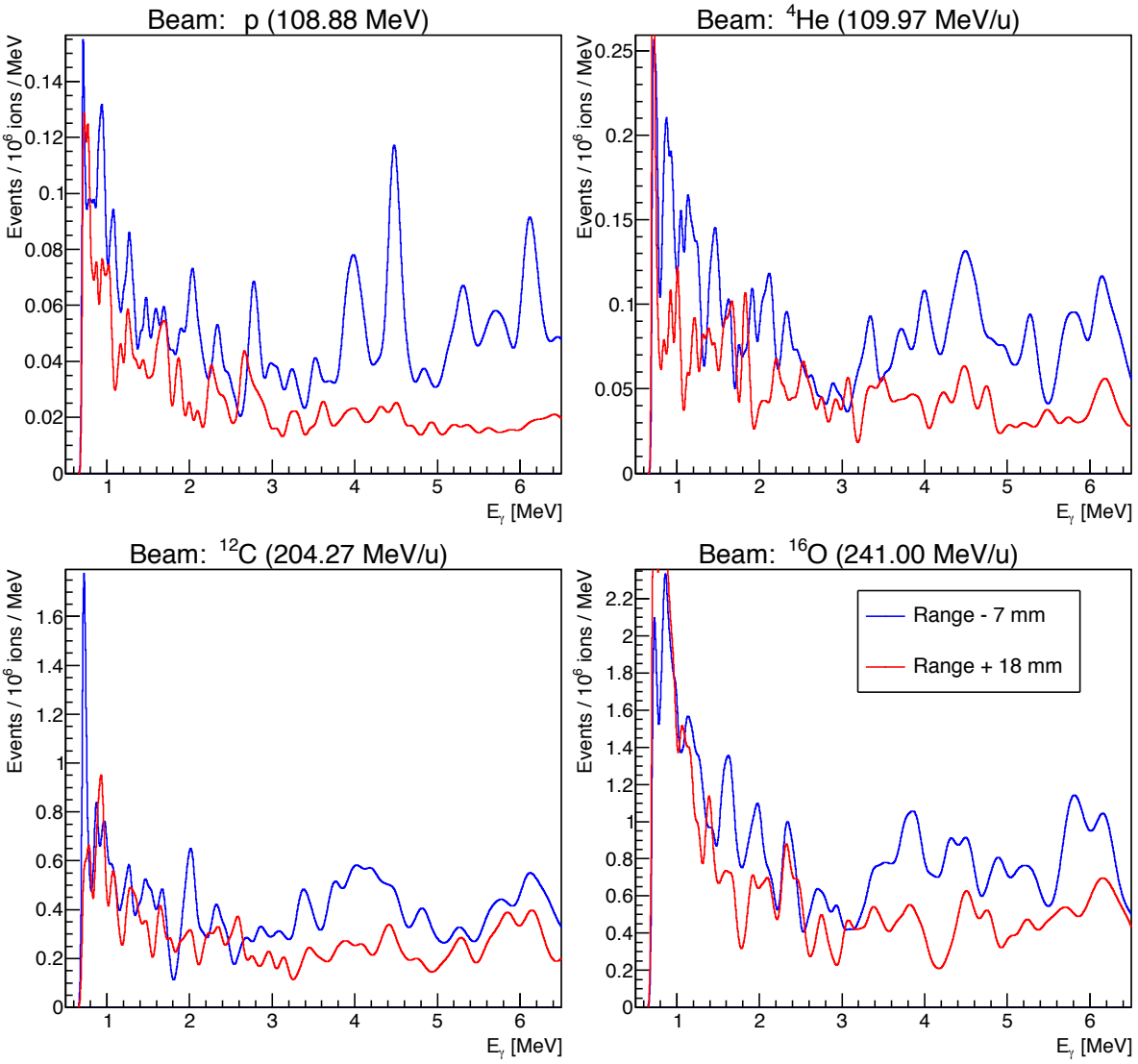

Figure 9. Energy spectra for the prompt gamma radiation before and after the Bragg peak obtained in the collimated experiments. The comparison between the four ion species is shown. The background has been suppressed after a full implementation of the background rejection techniques. The data was smoothed for better visualisation.

the $E_\gamma = 6.1$ MeV lines generated directly by ions traveling at a velocity compatible with a residual range of $r = 7$ mm. The predicted values and the measured ones were in agreement within the 1% level.

5.5.2. Scanning position The evolution of the intensities of the spectral lines for the collimated experiments in presence of the ^{12}C beam is presented in Figure 10. We analyzed 15 reactions identified in Table 2 and also the integrated spectrum between 0.6 MeV $\leq E_\gamma \leq$ 6.8 MeV. A correlation with the Bragg peak position was observed for each of the reactions. However, the specific shape and intensity was unique to each of the gamma lines. We can observe that, in general, the high energy lines reached

the maximum of the intensity just before the end of range and then they presented a sharp falloff. The behaviour at lower energies was more various and the maximum of the distribution was often reached at the Bragg peak position. A more detailed comparison between the intensities of these reactions is presented in Figure 11. Here, we can observe how the gamma lines at an intermediate energy present a common absolute intensity and a similar behaviour with respect to the depth in the phantom. On the other hand, differences were observed between the high and the low energy prompt gamma, which could provide valuable information to retrieve the absolute Bragg peak position. This result is compatible with the previous observations done in presence proton beams accelerated by cyclotrons by Verburg et al., 2014.

According to the findings described in the previous paragraph, we selected five independent pairs of prompt gamma lines from Figure 10 and we calculated $R_{j,k}$ at every position z_i. The results, including the propagation of the statistical errors and the parameterization of $R_{j,k}(z)$, are shown in Figure 12. We observed a monotonic relation between the depth in the water phantom z and the values assumed by the variables $R_{j,k}$ in a neighborhood of the Bragg peak. Therefore, the functional forms can be inverted and used to derive unequivocally the range of the primary beam. This, given the intensity of at least a pair of prompt gamma lines. We considered the ratio $R^{(1)} := I_{0.718\ \mathrm{MeV}}/I_{4.4\ \mathrm{MeV}}$ as an example to perform quantitative evaluations. The steepness of the curve at the Bragg peak position was $s^{(1)} = dR^{(1)}/dz = 0.03\ \mathrm{mm}^{-1}$ and the average statistical error of the data points in the neighborhood of the end of the range was $\bar{\sigma}(R^{(1)}) = 0.05$. Therefore, given one single measurement, the longitudinal position of the Bragg peak z_{BP} could be recovered with a statistical uncertainty of $\sigma(z_{BP}) = \bar{\sigma}(R^{(1)})/s^{(1)} = 1.67$ mm. Similar considerations applied to the other $R_{j,k}$ and the estimation of $\sigma(z_{BP})$ ranged from a minimum of 0.96 mm to a maximum of 3.89 mm for different pairs of gamma lines. The exact values of $s^{(i)}$ and $\bar{\sigma}(R^{(i)})$ for each pair of gamma lines are reported in Figure 12.

6. Discussion

In this work we have presented a small-scale prototype for absolute range verification of ion beams at synchrotron based facilities. The study was conducted using clinically relevant beam energies and intensities. The range verification technique was based on prompt gamma spectroscopy, which has already been demonstrated for proton beams accelerated at a cyclotron based facility by Hueso-González et al., 2018. We extended its applicability to a synchrotron based facility and heavier ions up to ^{16}O beams. This required the development of a dedicated detector system and data processing routines. Using this small-scale prototype, we demonstrated for the first time the possibility to measure the absolute Bragg peak position for ^{12}C beams accelerated by a synchrotron.

The development of prompt gamma spectroscopy for a synchrotron based facility and for ions heavier than protons posed several technical challenges, which we overcame. The differences with respect to cyclotrons in the time micro-structure of the beam

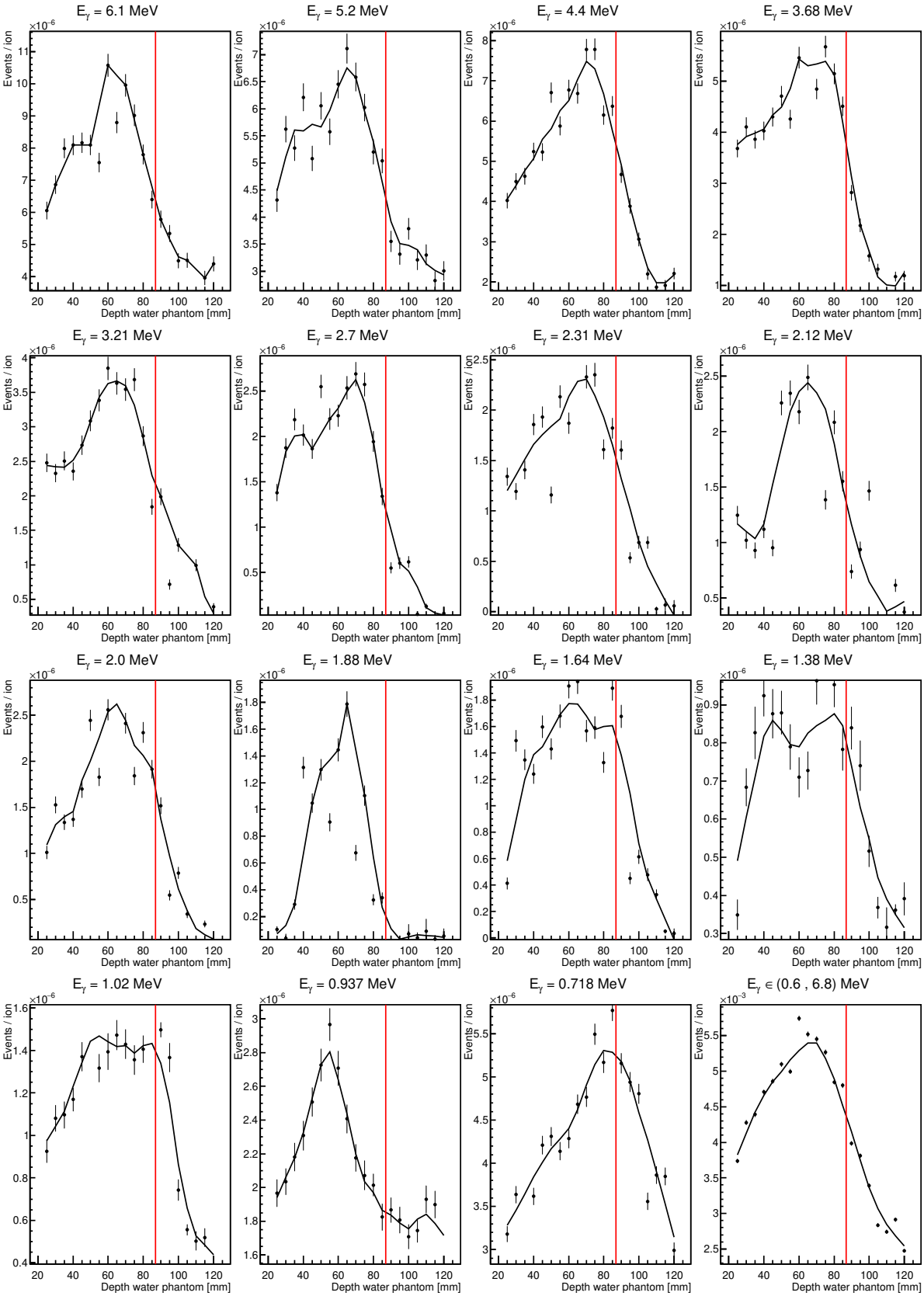

Figure 10. Evolution of the spectral lines intensities with respect to the longitudinal position of detection. The experimental data, obtained with ^{12}C beams in the collimated experiments, is shown with solid dots and its statistical uncertainty. The smoothed black lines help the reader to follow the data. The vertical red lines indicate the position of the Bragg peak.

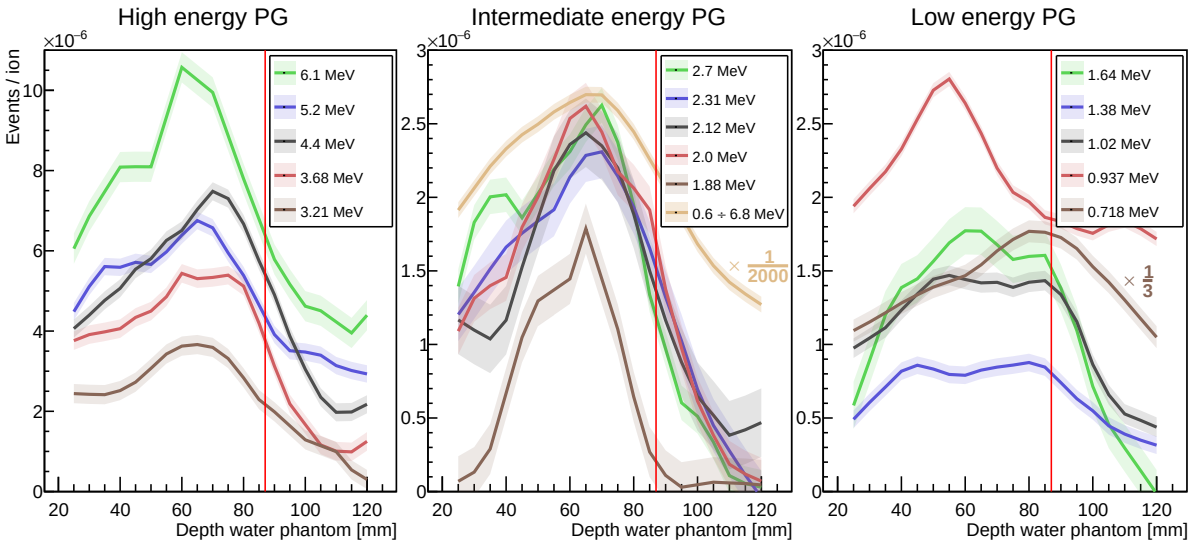

Figure 11. Comparison between multiple prompt gamma lines detected in presence of ^{12}C beams in the collimated experiments. The solid lines report the smoothed experimental data and the bands about these represent the average deviation from the original data points. Two lines were scaled to fit within the plots and their scaling factors are reported in the plot. The vertical red lines indicate the position of the Bragg peak.

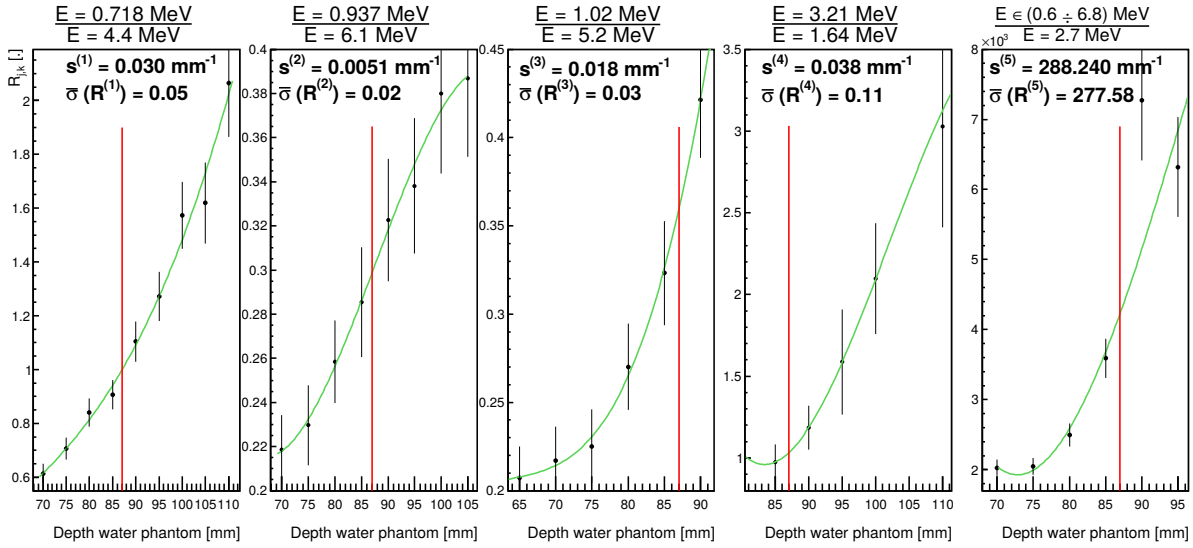

Figure 12. Ratios between the intensities of five pairs of prompt gamma lines. The experimental data is shown with solid dots and its statistical uncertainty. The green curves are the polynomial fit of the experimental data and the vertical red lines indicate the position of the Bragg peak. The variables $s^{(i)}$ and $\bar{\sigma}(R^{(i)})$ indicate respectively the steepness of the polynomial fit at the Bragg peak position and the mean statistical uncertainty of the data points in a 1 cm neighborhood of it.

requires a different approach to perform background rejection through a ToF model. Therefore, we developed and implemented in the experimental setup a dedicated beam trigger. Both the EJ-200 detector and the SciFi detector were capable to track the arrival time of single ions. We achieved a time resolution down to FWHM $\simeq$ 1 ns (Figure 8). The SciFi detector was designed to have minimal interaction with the beam, to operate at high beam intensities and to be scalable to the highest intensities during patient treatments at HIT (Magalhaes Martins et al., 2019). The possible implementation of scintillating fiber detectors in the nozzle for patient treatments was discussed by Leverington et al., 2018. Second, we implemented a series of robust background rejection techniques. The first steps were based on the information retrieved by the secondary detectors. Dal Bello et al., 2019 demonstrated that the anti-coincidence detection provides convergence in the estimation of the peaks intensities starting from 10^5 events in the $CeBr_3$, which is one order of magnitude smaller than the amount of events acquired during the current study in the collimated experiments and two orders of magnitude for the uncollimated experiments. We implemented also further steps based on the detector and the ToF spectra modelling. The detector effects (e.g. Compton continuum) and the neutron induced background (e.g. spectral line at $E_\gamma = 2.2$ MeV) were suppressed. The excellent time resolution achieved with the SciFi detector was exploited to develop a ToF model describing the characteristics of the time spectra generated by a synchrotron beam with a minimal set of free parameters. The robustness of the model was tested by performing unsupervised fits of the ^{12}C time spectra at the different z_i positions down-sampling the statistics to approximately $8 \cdot 10^5$ events, which properly described the data (not shown). An exemplary fit was shown in Figure 3. In Appendix B is shown that 10^9 primary ^{12}C ions could be found only for the total plan and fewer particles are normally delivered to a single layer during one fraction. As discussed below, an improvement of the detector sensitivity will be required to achieve small statistical errors of the Bragg peak position measurement. Such improvement would also lead to detect more events with the PGS system, even if starting from a smaller number of primary ions. Therefore, the background suppression techniques will be applied to data sets with a number of events sufficiently high to fall within the range where the robustness of the fitting routines was verified during this work.

The background rejection allowed to extract parameters from the time and energy spectra, which we then correlated with the residual range of the primary ^{12}C ions. We identified in total 19 independent spectral lines induced by the four beam species on the different targets. Some of the lines were unique to target nuclei found in artificial implants but not in human tissue, in this specific case the titanium. The detection of such reactions could potentially be used to identify whether the beam path crosses a metallic implant, as proposed for ^{4}He beams in Dal Bello et al., 2019. In the current work, we demonstrated this technique also for p, ^{12}C and ^{16}O beams. Moreover, we observed that several spectral lines were generated by decays between multiple excited states without reaching directly the ground state, e.g. the chain $^{10}B^*_{3.59} \rightarrow {}^{10}B^*_{0.718} \rightarrow {}^{10}B_{g.s.}$ produces two gamma quanta at $E_\gamma^{(1)} = 2.7$ MeV and

$E_\gamma^{(2)} = 0.718$ MeV in coincidence. The direct detection of such coincidences was not investigated in the current work. Similar prompt gamma emission chains could be identified in Table 2. Such reactions, in presence of multiple spectroscopic units, open the possibility to retrieve the transverse position of the prompt gamma production (Panaino et al., 2018). The $E_\gamma = 0.511$ MeV line was also detected but not analyzed. Furthermore, the background-suppressed spectra were used to perform a quantitative analysis of the Doppler broadening. We observed that the model derived in Appendix A successfully described the experimental data. The magnitude of the effect was larger on the high energy lines compared to the low energy ones, as shown in Figure 7. Therefore, the capability to detect the low energy gamma lines is beneficial for a range verification system, especially in presence of ^{12}C and ^{16}O beams for which the widening of the spectral lines reached its maximum. For ^{12}C and ^{16}O beams we also observed the direct prompt gamma emission from the projectiles in Figure 9. The position of the Doppler shifted peaks could potentially be used to invert the equations (4)-(9) and directly measure the residual beam energy, i.e. the residual range. However, we expect such technique not to be exploitable at the end of the range. Here, the Doppler shifts reach their minima and the peaks merge with the emission lines from the target nuclei. Nonetheless, such information could be used to obtain an independent check on whether the detection is compatible with the z ranges of Figure 12.

The influence of the longitudinal detection coordinate with respect to the Bragg peak position was observed in the ToF spectra in Figure 8 and the energy spectra in Figure 9. We interpret the differences observed in the ToF spectra between the lightest (p and ^{4}He) and the heavier (^{12}C and ^{16}O) beams due to the fragmentation of the primary particles. For the latter, the light fragments produced before the Bragg peak travel also beyond it, exciting target nuclei and generating prompt gamma in the primary ToF peak also at $z = 105$ mm. This interpretation was supported by the spectra in Figure 9. Here, we observed that at $z = 105$ mm the de-excitation lines of the target nuclei are still present, while the Doppler shifted emission from the ^{12}C and ^{16}O projectiles vanished. Another difference in the ToF spectra was given by the number of events in the $f_S(t)$ component. This was compatible with the expected lower neutron production for p and ^{4}He beams, which led to fewer (n, γ) reactions. The presence of a large background from (n, γ) reactions delayed by just $\Delta t \simeq 3$ ns from the prompt gamma peak requires the adoption of a dedicated beam trigger with high time resolution, especially for ^{12}C and ^{16}O beams.

The correlation of spectral parameters with the Bragg peak position was investigated in detail in presence of ^{12}C beams. We characterized the intensity of the prompt gamma lines at different depths in the phantom and presented the results in Figure 10 and Figure 11. We interpret the distinct behaviours between separate gamma lines due to the differences in the cross sections for the production of the nuclear excited states. Interestingly, the low energy gamma emissions reach their maximum intensities at the Bragg peak, i.e. where the primary ^{12}C is almost at rest. We interpret this effect assuming that the energy thresholds for such nuclear reactions are at a lower energy

compared to the processes generating high energy prompt gamma. Such property could be beneficial to detect the residual range in a neighborhood of the Bragg peak. It has to be reminded that the steepness of the curves is a combination of the intrinsic drop of intensity at the Bragg peak with the transfer function through the slit collimator, which was not optimized during this work. We also observed that, oppositely to the results presented by Verburg et al., 2014, the counts of the spectral lines do not drop to zero after the end of range. Again, we interpret this with the presence of nuclear fragments produced by the ^{12}C projectile, which are not created by p beams. Nonetheless, it was possible to detect a correlation between the spectral line intensities and the absolute Bragg peak position. We chose to calculate the ratios $R_{j,k}(z_i)$ to suppress possible systematic errors and biases introduced during the post-processing. The ten independent spectral lines used to calculate the five ratios in Figure 12 allowed to develop a method capable to retrieve the absolute position of the Bragg peak. The functional forms $r_{j,k}(z)$ describing the data $R_{j,k}(z_i)$ were monotonic and therefore unequivocally invertible. The existence of the inverse function $z_{j,k}(R) = r_{j,k}^{-1}(R)$ in a neighborhood of the Bragg peak is sufficient to mathematically demonstrate that its absolute position can be retrieved analyzing the prompt gamma spectrum. The presented work was based on one single set of measurements. Therefore, while the existence of $z_{j,k}(R)$ was demonstrated, the method was not tested on an independent data point to perform an end-to-end absolute range measurement. Nonetheless, this finding encourages further development of PGS for ^{12}C ion beams towards a pre-clinical prototype.

A possible future application of this technique during treatment will require a detailed knowledge of the cross sections for the reactions listed in Table 2 together with the modelling of the attenuation of the gamma radiation in the patient and the interaction with the detector system. The ^{12}C and ^{16}O concentrations in the target can be derived analyzing the prompt gamma spectra (Hueso-González et al., 2018). The properties of the mixed field of ^{12}C and fragments should be calculated at every depth with Monte Carlo or analytic software, e.g. FRoG (Mein et al., 2018). Prior to the treatment, the patient specific $r_{j,k}(z)$ should be calculated along with their inverse functions $r_{j,k}^{-1}(R)$. During the treatment, the spectroscopic unit would be placed at one specific depth to measure one or more $\hat{R}_{j,k} = R_{j,k}(\hat{z})$ values. The absolute Bragg peak position is then promptly estimated from the value assumed by $r_{j,k}^{-1}(\hat{R}_{j,k})$. The precision of the range estimation depends primarily on the steepness $dr_{j,k}/dz$ and the statistical uncertainty of $\hat{R}_{j,k}$. We demonstrated submillimetric range verification with experimental data using ^{12}C beams stopped in a water phantom. In this case, the functions $r_{j,k}(z)$ were defined empirically from the experimental data itself.

The current version of the PGS system achieved a submillimetric statistical precision with $N_0 = 8 \cdot 10^9$ primary ^{12}C ions. In the following discussion we extrapolate the requirements for a future full scale prototype aiming to retrieve the Bragg peak position with a confidence interval of $\sigma(z_{BP}) = 2$ mm. Such precision should be compared to the intrinsic width of the Bragg peak falloff. For the maximum energies available at HIT, the range straggling contributes less than 2 mm for ^{12}C and ^{16}O ions,

approximately 2 mm for ^{4}He ions and it overcomes this width for an initial energy above 150 MeV for proton beams. The following considerations are developed for ^{12}C beams taking the $R^{(1)}$ experimental data is taken as an example. Given the $1.2 \cdot 10^{6}$ events detected by the spectroscopic unit and the fact that the statistical uncertainty scales with $\sigma(z_{BP}) \propto 1/\sqrt{N_{\gamma}}$; the number of detected events required to achieve the desired precision is approximately $8 \cdot 10^{5}$. The relations between the dose delivered, the number of ions used and the amount of gamma events are derived in the Appendix B. The verification of the range on a spot-by-spot basis is impracticable for a single fraction delivery of $D = 2$ Gy physical dose. Techniques such as spot merging would be required. In this case, we sum the statistics provided by all the particles delivered within a circle of radius $\xi = 15$ mm on a transverse plane (x, y) of the most distal layer. It is important to remark that this work was primarily focused on ^{12}C beams and therefore the extrapolation to the other ion species is discussed but can only be preliminary. We observe that to obtain a confidence interval of $\sigma(z_{BP}) = 2$ mm during a $D = 2$ Gy physical dose delivery, the efficiency of the PGS system should be increased by a factor between $\times 15$ and $\times 40$ depending on the selected ion. The highest sensitivity improvement would be required for ^{12}C ions. We foresee that improving detection efficiency by an order of magnitude is practicable for a full scale system, e.g. adopting multiple spectroscopic units or larger $CeBr_3$ crystals. The optimization of the collimator geometry would also ease the statistical requirements. Moreover, one could simultaneously extrapolate the range from all the independent $R_{j,k}$ estimators or with a direct comparison of the data to pre-calculated range shift scenarios. This is expected to improve the efficiency up to a factor five given that so many different ratios $R_{j,k}$ were found to be monotonically related to the Bragg peak position. We can conclude that, despite the challenges associated to the improvement of the sensitivity in a full scale prototype, measuring the absolute Bragg peak position with a statistical precision of $\sigma(z_{BP}) = 2$ mm during the delivery of $D = 2$ Gy physical dose to an homogeneous water phantom is within reach. The investigation of the performances of the system with varying elemental composition of the target and in presence of complex geometries is of interest for the clinical applicability of the method but was beyond the scope of this work and will be investigated in future studies.

7. Conclusions

The experimental investigation of prompt gamma spectroscopy at a synchrotron based facility was presented. The features of the time and energy spectra for the prompt gamma radiation generated by p, ^{4}He, ^{12}C and ^{16}O beams were investigated before and after the Bragg peak, showing a correlation between the detection position and the range of the primary particles for all ion species. The existence of invertible functions that correlate the Bragg peak position to features extracted from the prompt gamma energy spectra was demonstrated for the first time for ^{12}C beams. The influence of the Doppler broadening and the effect of light fragments on the energy spectra were quantified and

did not prevent the development of a method to retrieve the residual range of the primary beam particles through prompt gamma spectroscopy. The promising results encourage future work, which will start from the cross sections measurement.

Acknowledgments

Author R.D.B. is supported by the International Max Planck Research School for Quantum Dynamics in Physics, Chemistry and Biology, Heidelberg, Germany. P.M.M. is supported by a research fellowship for postdoctoral researchers from the Alexander von Humboldt Foundation, Bonn, Germany. The authors thank the radiation protection department of the DKFZ, in particular Mechthild Kämmer, for the support with calibration sources. The authors also thank the staff of the department of medical physics in radiation oncology of the DKFZ, in particular Gernot Echner, Armin Runz and Peter Häring for the support with the experimental setup.

Appendix A

In this appendix we derive the equations that describe the influence of the Doppler effect on the detected spectra. Two separate effects are derived for the collimated and the uncollimated experiments. In the former, we derive the Doppler shift of the radiation emitted by the excited projectile at a well defined residual kinetic energy. In the latter, we approximate the Doppler broadening by averaging over multiple Doppler shifts of the radiation emitted in center of mass of the collision.

Let us first consider the collimated case, where the residual kinetic energy of the projectile is known. Moreover, we consider the emission of the prompt gamma only from the excited projectiles ^{12}C and ^{16}O and not from the target nuclei. A photon of energy E_0 emitted by an excited nucleus moving at speed β with respect to the laboratory frame is detected at an angle θ with an energy E_m given by

$$E_m = E_0 \cdot \frac{\sqrt{1-\beta^2}}{1-\beta\cdot\cos\theta} \tag{4}$$

in our experiments we have the condition $\theta = \frac{\pi}{2}$ and the equation (4) reduces to

$$E_m = E_0 \cdot \frac{\sqrt{1-\beta^2}}{1-\beta\cdot\cos\frac{\pi}{2}} = E_0 \cdot \sqrt{1-\beta^2} = \frac{E_0}{\gamma}. \tag{5}$$

The data upstream the Bragg peak presented in Figure 9 has been measured where the residual range of the primary ions was $R_r = 7$ mm, which correspond to

$$E_{kin}(^{12}\mathrm{C}) = 48 \text{ MeV/u} \quad \longrightarrow \quad \gamma(^{12}\mathrm{C}) = 1.0515 \tag{6}$$

$$E_{kin}(^{16}\mathrm{O}) = 56 \text{ MeV/u} \quad \longrightarrow \quad \gamma(^{16}\mathrm{O}) = 1.0601. \tag{7}$$

We consider the arithmetic average of the gamma quanta emitted by the merged reactions at $E_0^{(1)} = 4.445$ MeV and $E_0^{(2)} = 6.155$ MeV, respectively by the projectiles ^{12}C and ^{16}O. These are detected in the laboratory rest frame at a lower energy according to (5)-(7), obtaining

$$E_m^{(1)} = 4.445 \text{ MeV}/1.0515 = 4.227 \text{ MeV} \quad \longrightarrow \quad \Delta E^{(1)} = 0.218 \text{ MeV} \tag{8}$$

$$E_m^{(2)} = 6.155 \text{ MeV}/1.0601 = 5.806 \text{ MeV} \quad \longrightarrow \quad \Delta E^{(2)} = 0.349 \text{ MeV}. \tag{9}$$

A different situation is present in the uncollimated experiments. Here, the kinetic energy of the projectile inducing prompt gamma production spans from the maximum beam energy to zero. We also consider the emission of the gamma quanta by the target nuclei. The net effect is the superposition of multiple Doppler shifted peaks in the spectrum and therefore wider spectral lines. Let us first calculate the center of mass energy of a collision between a generic projectile of mass $m_p = A \cdot u$ having total energy $E_A = \gamma_p \cdot A \cdot u$ with a ^{16}O target nucleus of mass $m_t = 15.9949 \cdot u \simeq 16 \cdot u$

$$E_{CM}^2 = s^2 = \left[\begin{pmatrix} E_A \\ \vec{p}_A \end{pmatrix}^2 + \begin{pmatrix} 16\cdot u \\ 0 \end{pmatrix}^2 \right] = (A\cdot u)^2 + (16\cdot u)^2 + 32\cdot\gamma_p\cdot A\cdot u^2. \tag{10}$$

The equation (10) can be used to calculate the Lorentz factor of frame moving with the center of mass

$$\gamma_{CM} = \frac{E_{CM}}{(16+A)\cdot u} = \frac{\sqrt{A^2+16^2+32\cdot\gamma_p\cdot A}}{16+A}. \tag{11}$$

We observe that for the data presented in Figure 6 the projectiles have an initial energy corresponding to a maximum $\gamma_p^{max} = 1.35$ for ^{16}O and a minimum $\gamma_p^{min} = 1.15$ for p. In (11) we approximate $\gamma_p \simeq \bar{\gamma}_p := 0.5\cdot(\gamma_p^{max}+\gamma_p^{min}) = 1.25$. We also approximate the total widening of the spectral line having nominal energy E_0 with a linear relation to the Doppler shift, namely

$$FWHM \simeq \kappa\cdot|E_m - E_0|. \tag{12}$$

Plugging (5) and (11) into (12) we obtain

$$FWHM = \kappa\cdot E_0\cdot\frac{\sqrt{A^2+16^2+32\cdot\bar{\gamma}_p\cdot A}-16-A}{\sqrt{A^2+16^2+32\cdot\bar{\gamma}_p\cdot A}} \tag{13}$$

to describe the widening of the spectral lines with increasing mass of the projectile. This effect can be seen as a direct consequence of the greater center of mass velocities for heavier projectiles.

Ion	$\sum_{IES} N_0(IES)$	$N_0(IES = 17)$	$\rho\,[\text{ions} \cdot \text{mm}^{-2}]$	$N_\gamma(\xi = 5 \cdot \Delta x)$	$\hat{\epsilon}$
p	$2.73 \cdot 10^{10}$	$7.44 \cdot 10^{9}$	$2.98 \cdot 10^{6}$	$5.48 \cdot 10^{4}$	15.3
^{4}He	$7.22 \cdot 10^{9}$	$2.06 \cdot 10^{9}$	$8.25 \cdot 10^{5}$	$2.45 \cdot 10^{4}$	34.2
^{12}C	$1.34 \cdot 10^{9}$	$3.59 \cdot 10^{8}$	$1.44 \cdot 10^{5}$	$2.04 \cdot 10^{4}$	41.1
^{16}O	$8.68 \cdot 10^{8}$	$2.42 \cdot 10^{8}$	$9.69 \cdot 10^{4}$	$2.88 \cdot 10^{4}$	29.1

Table 3. Properties of the treatment plans delivering a $D = 2$ Gy dose box. The columns report in order: the total number of ions irradiated, the ions in the most distal layer, the transverse ion density in the most distal layer, the estimated number of gamma for a spot merging of radius $\xi = 5 \cdot \Delta x$ and the improvement of the detection efficiency required to reach $\sigma(z_{BP}) = 2$ mm.

Appendix B

In this appendix we derive the relations between the dose, the number of ions irradiated and the statistical requirements for the range measurements. We used the treatment planning system syngo.via¶ to calculate four plans delivering uniform dose boxes to a volume $V = 50 \times 50 \times 50$ mm^3 for the ions used in the current study. We chose to deliver $D = 2$ Gy physical dose in accordance to the single fraction delivery used in previous studies (Richter et al., 2016). We calculated the plans for p, ^{4}He, ^{12}C and ^{16}O beams with identical properties, namely: $\Delta x = \Delta y = 3$ mm transverse spacing between the single spots and $N_{IES} = 17$ iso-energy slices (IES). The deepest IES corresponded to the energy used in the collimated experiments. Each plan had a total of $N_P = 4913$ points, of which $N_P/N_{IES} = 289$ at the most distal layer. The number of particles irradiated was uniformly distributed among the pencil beam points in each IES. Further properties of the plans are summarized in Table 3. The most fundamental parameter for statistical considerations is the transverse ion density ρ irradiated to the most distal layer. While the number of particles per single spot depends on other parameters (e.g. Δx), the value of ρ is in first approximation constant. Assuming a uniform distribution in a small transverse neighborhood, we can calculate the estimated number of gamma that would be measured with the current setup for a spot merging of radius $\xi = 5 \cdot \Delta x$. This integration radius is slightly larger to the one adopted in previous studies (Hueso-González et al., 2018) but it has to be reminded that in our calculation we did not merge the statistics accumulated in the longitudinal direction z. The values $N_\gamma(\xi = 5 \cdot \Delta x)$ are calculated taking as a reference the $1.2 \cdot 10^{6}$ events measured in the spectroscopic unit with $8 \cdot 10^{9}$ primary ^{12}C ions and then scaled to the other ion species according to the $\Gamma_{^{12}C,i}$ factors. Finally, the improvement of the detection efficiency required to reach $\sigma(z_{BP}) = 2$ mm is calculated assuming that $8.37 \cdot 10^{5}$ events should be detected by the PGS system to achieve such confidence interval. We observe that the values of $\hat{\epsilon}$ range from approximately 15 to 40, they are minimum for the proton beams and maximum for the ^{12}C ions.

¶ Siemens Healthcare GmbH, Erlangen, Germany

References

Amaldi, Ugo et al. (Aug. 2005). "Radiotherapy with beams of carbon ions". In: *Reports on Progress in Physics* 68.8, pp. 1861–1882. ISSN: 0034-4885. DOI: 10.1088/0034-4885/68/8/R04. URL: http://stacks.iop.org/0034-4885/68/i=8/a=R04?key=crossref.9a0f1e1c20da5f308fd7ce9a8adad161.

Aricò, G et al. (Mar. 2019). "Investigation of single carbon ion fragmentation in water and PMMA for hadron therapy". In: *Physics in Medicine & Biology* 64.5, p. 055018. ISSN: 1361-6560. DOI: 10.1088/1361-6560/aafa46. URL: http://stacks.iop.org/0031-9155/64/i=5/a=055018?key=crossref.3ff6790bd1475297d1a043666ced7ce9.

Böhlen, T.T. et al. (June 2014). "The FLUKA Code: Developments and Challenges for High Energy and Medical Applications". In: *Nuclear Data Sheets* 120, pp. 211–214. ISSN: 00903752. DOI: 10.1016/j.nds.2014.07.049. URL: https://linkinghub.elsevier.com/retrieve/pii/S0090375214005018.

Bragg, W. H. et al. (Sept. 1905). "On the alpha particles of radium, and their loss of range in passing through various atoms and molecules". In: *The London, Edinburgh, and Dublin Philosophical Magazine and Journal of Science* 10.57, pp. 318–340. DOI: 10.1080/14786440509463378. URL: https://www.tandfonline.com/doi/full/10.1080/14786440509463378.

Brun, Rene et al. (Apr. 1997). "ROOT — An object oriented data analysis framework". In: *Nuclear Instruments and Methods in Physics Research Section A: Accelerators, Spectrometers, Detectors and Associated Equipment* 389.1-2, pp. 81–86. ISSN: 0168-9002. DOI: 10.1016/S0168-9002(97)00048-X. URL: https://www.sciencedirect.com/science/article/pii/S016890029700048X?via%3Dihub.

Castriconi, Roberta et al. (Jan. 2017). "Dose-response of EBT3 radiochromic films to proton and carbon ion clinical beams". In: *Physics in Medicine and Biology* 62.2, pp. 377–393. ISSN: 13616560. DOI: 10.1088/1361-6560/aa5078.

Dal Bello, Riccardo et al. (Apr. 2018). "CeBr3 scintillators for 4He prompt gamma spectroscopy: Results from a Monte Carlo optimization study". In: *Medical Physics* 45.4, pp. 1622–1630. ISSN: 00942405. DOI: 10.1002/mp.12795.

Dal Bello, Riccardo et al. (May 2019). "Results from the experimental evaluation of CeBr3 scintillators for 4He prompt gamma spectroscopy". In: *Medical Physics* 46.8, pp. 3615–3626. DOI: 10.1002/mp.13594. URL: https://onlinelibrary.wiley.com/doi/abs/10.1002/mp.13594.

Ferrari, Alfredo et al. (2005). *FLUKA: A multi-particle transport code (Program version 2005)*. URL: http://inspirehep.net/record/701721?ln=it.

Guttormsen, M et al. (1996). *The unfolding of continuum γ-ray spectra*. Tech. rep., pp. 371–376.

Haberer, Th. et al. (Dec. 2004). "The heidelberg ion therapy center". In: *Radiotherapy and Oncology* 73, S186–S190. ISSN: 0167-8140. DOI: 10.1016/S0167-8140(04)

80046-X. URL: https://www.sciencedirect.com/science/article/pii/S016781400480046X?via%3Dihub.

Hueso-González, Fernando et al. (Sept. 2018). "A full-scale clinical prototype for proton range verification using prompt gamma-ray spectroscopy". In: *Physics in Medicine and Biology* 63.18. ISSN: 13616560. DOI: 10.1088/1361-6560/aad513.

Kelleter, Laurent et al. (Feb. 2017). "Spectroscopic study of prompt-gamma emission for range verification in proton therapy". In: *Physica Medica* 34, pp. 7–17. ISSN: 1724191X. DOI: 10.1016/j.ejmp.2017.01.003.

Kinsey, R R (1998). "The NUDAT/PCNUDAT Program for Nuclear Data". In: *IAEA-NDS-162* 27.1. URL: http://www-nds.iaea.or.at.

Knopf, Antje Christin et al. (Aug. 2013). *In vivo proton range verification: A review*. DOI: 10.1088/0031-9155/58/15/R131.

Kozlovsky, Benzion et al. (Sept. 2002). "Nuclear Deexcitation Gamma-Ray Lines from Accelerated Particle Interactions". In: *The Astrophysical Journal Supplement Series* 141.2, pp. 523–541. ISSN: 0067-0049. DOI: 10.1086/340545.

Krimmer, J. et al. (Jan. 2018). *Prompt-gamma monitoring in hadrontherapy: A review*. DOI: 10.1016/j.nima.2017.07.063.

Leverington, B.D. et al. (May 2018). "A prototype scintillating fibre beam profile monitor for Ion Therapy beams". In: *Journal of Instrumentation* 13.05, P05030–P05030. ISSN: 1748-0221. DOI: 10.1088/1748-0221/13/05/P05030. URL: http://stacks.iop.org/1748-0221/13/i=05/a=P05030?key=crossref.f525aab76f0a1bad8ce7b3b9c7fa997a.

Magalhaes Martins, Paulo et al. (Jan. 2017). "Prompt gamma spectroscopy for range control with CeBr3". In: *Current Directions in Biomedical Engineering* 3.2, pp. 113–117. DOI: 10.1515/cdbme-2017-0023. URL: http://www.degruyter.com/view/j/cdbme.2017.3.issue-2/cdbme-2017-0023/cdbme-2017-0023.xml.

Magalhaes Martins, Paulo et al. (2019). *Hadron beam time tracker for time-of-flight measurements of prompt-gamma*. Tech. rep. GSI-2019-00596. DOI: 10.15120/GSI-2019-00596. URL: https://www.gsi.de/fileadmin/Biophysik/Bilder/Bilder_Gallery/Biophysics_Collaboration/Final_Version_web_version.pdf.

Mein, Stewart et al. (2018). "Fast robust dose calculation on GPU O ion therapy : the FRoG platform". In: pp. 1–12. DOI: 10.1038/s41598-018-33194-4.

Mein, Stewart et al. (Dec. 2019). "Biophysical modeling and experimental validation of relative biological effectiveness (RBE) for 4He ion beam therapy". In: *Radiation Oncology* 14.1, p. 123. ISSN: 1748-717X. DOI: 10.1186/s13014-019-1295-z. URL: https://ro-journal.biomedcentral.com/articles/10.1186/s13014-019-1295-z.

Paganetti, Harald (June 2012). *Range uncertainties in proton therapy and the role of Monte Carlo simulations*. DOI: 10.1088/0031-9155/57/11/R99.

Panaino, C. et al. (Jan. 2018). "Abstract ID: 171 A Monte Carlo study to reduce range uncertainty in proton beam therapy via prompt gamma-ray detection". In: *Physica Medica* 45, S2. ISSN: 1120-1797. DOI: 10.1016/J.EJMP.2017.11.027. URL: https:

//www.sciencedirect.com/science/article/abs/pii/S1120179717306221?via%3Dihub.

Pinto, M et al. (Jan. 2015). "Absolute prompt-gamma yield measurements for ion beam therapy monitoring". In: *Physics in Medicine and Biology* 60.2, pp. 565–594. ISSN: 0031-9155. DOI: 10.1088/0031-9155/60/2/565. URL: http://stacks.iop.org/0031-9155/60/i=2/a=565?key=crossref.c4760640602341dfb0ce09b91884d4e4.

PTCOG (2018). *Particle Therapy Patient Statistics (per end of 2018)*. URL: https://www.ptcog.ch/images/patientstatistics/Patientstatistics-updateDec2018.pdf.

Quarati, F G A et al. (Nov. 2013). "Scintillation and detection characteristics of high-sensitivity CeBr3 gamma-ray spectrometers". In: *Nuclear Instruments and Methods in Physics Research Section A: Accelerators, Spectrometers, Detectors and Associated Equipment* 729, pp. 596–604. DOI: 10.1016/J.NIMA.2013.08.005. URL: https://www.sciencedirect.com/science/article/pii/S0168900213011297?via%3Dihub.

Richter, Christian et al. (Feb. 2016). "First clinical application of a prompt gamma based in vivo proton range verification system." In: *Radiotherapy and oncology : journal of the European Society for Therapeutic Radiology and Oncology* 118.2, pp. 232–7. ISSN: 1879-0887. DOI: 10.1016/j.radonc.2016.01.004. URL: http://www.ncbi.nlm.nih.gov/pubmed/26774764.

Roemer, K. et al. (Oct. 2015). "Characterization of scintillator crystals for usage as prompt gamma monitors in particle therapy". In: *Journal of Instrumentation* 10.10, P10033–P10033. ISSN: 1748-0221. DOI: 10.1088/1748-0221/10/10/P10033. URL: http://stacks.iop.org/1748-0221/10/i=10/a=P10033?key=crossref.97faf45643409837756a2a2493868c0e.

Testa, M. et al. (Aug. 2010). "Real-time monitoring of the Bragg-peak position in ion therapy by means of single photon detection". In: *Radiation and Environmental Biophysics* 49.3, pp. 337–343. ISSN: 0301634X. DOI: 10.1007/s00411-010-0276-2.

Tommasino, Francesco et al. (Oct. 2015). "New Ions for Therapy". In: *International Journal of Particle Therapy* 2.3, pp. 428–438. ISSN: 2331-5180. DOI: 10.14338/ijpt-15-00027.1.

Vanstalle, Marie et al. (Aug. 2017). "Benchmarking Geant4 hadronic models for prompt γ monitoring in carbon ion therapy". In: *Medical Physics* 44.8, pp. 4276–4286. DOI: 10.1002/mp.12348. URL: https://onlinelibrary.wiley.com/doi/abs/10.1002/mp.12348.

Verburg, Joost M. et al. (Oct. 2013). "Energy- and time-resolved detection of prompt gamma-rays for proton range verification". In: *Physics in Medicine and Biology* 58.20. ISSN: 00319155. DOI: 10.1088/0031-9155/58/20/L37.

Verburg, Joost M. et al. (Dec. 2014). "Proton range verification through prompt gamma-ray spectroscopy". In: *Physics in Medicine and Biology* 59.23, pp. 7089–7106. ISSN: 13616560. DOI: 10.1088/0031-9155/59/23/7089.

Werner, F. et al. (Dec. 2017). "Performance verification of the FlashCam prototype camera for the Cherenkov Telescope Array". In: *Nuclear Instruments and Methods in Physics Research Section A: Accelerators, Spectrometers, Detectors and Associated Equipment* 876, pp. 31–34. ISSN: 0168-9002. DOI: 10.1016/J.NIMA.2016.12.056. URL: https://www.sciencedirect.com/science/article/pii/S0168900216313225?via%3Dihub.

Xie, Yunhe et al. (2017). "Prompt Gamma Imaging for In Vivo Range Verification of Pencil Beam Scanning Proton Therapy". In: 99.1, pp. 210–218. DOI: 10.1016/j.ijrobp.2017.04.027.